

**Probing the Quantum
Nature of Fe₈ High Spin
Molecules Using μ SR**

Oren Shafir

**Probing the Quantum Nature of Fe₈ High Spin
Molecules Using μ SR**

RESEARCH THESIS

SUBMITTED IN PARTIAL FULFILLMENT OF THE
REQUIREMENTS FOR THE DEGREE OF MASTER OF
SCIENCE IN PHYSICS

OREN SHAFIR

SUBMITTED TO THE SENATE OF THE TECHNION - ISRAEL INSTITUTE OF TECHNOLOGY

SHVAT , 5764

HAIFA

FEBRUARY, 2004

The research thesis was done under the supervision of Prof. Amit Keren in the faculty of physics.

I am deeply grateful to Prof. Amit Keren for his excellent guidance, his support and encouragement throughout this period.

I thank Prof. E. Polturak and Prof. M. Reznikov for their help with the DR. I appreciate very much the help of Dr. Y. Sheynin, Dr. M. Kapon and Prof. M. Kaftori with sample preparation and characterization. Great thanks also to Prof. S. Maegawa and Dr. M. Ueda for initial samples and for Dr. Ueda for her help with the thesis writing. For μ SR instrument support I want to thank Dr. A. Amato and C. Bains.

I am grateful for the big help from the lab technicians - Galina Bazalitzky, Mordechai Ayalon, Shmuel Hoida and Dr. Leonid Iomin. I want to thank also Dr. Salman for his help in the first steps.

Thanks to all my friends in the research group of magnetism and Low temperatures – Dr. Amit Knigel, Eva, Rinat, Oshri, Ariel, Lior, Shahar and Meni for their help and the wonderful working atmosphere they created.

Special and final thank to Bilha, the person who stood beside me and made this period of time more than studying.

The generous financial help of the Technion is gratefully acknowledged.

To my parents, Tami and Nisim, for their unconditional love and support

Contents

Abstract	-1-
List of symbols and abbreviations	-3-
1. Preface	-5-
1.1 Introduction - high spin molecules (HSM)	-5-
1.2 Quantum tunneling of the magnetization (QTM) in Fe8	-5-
1.3 Motivation for this work	-8-
2. Quantum Tunneling In High Spin Molecules	-10-
2.1 Tunneling between degenerate states	-10-
2.2 \mathcal{H}_0 and Magnetic Relaxation	-11-
2.3 The tunneling process	-12-
2.4 Tunneling in non-zero external magnetic fields	-14-
2.5 Landau Zener method	-15-
3. Experimental methods	-17-
3.1 Sample preparation	-17-
3.1.1 Chemical analysis	-18-
3.1.2 X-ray crystallography analysis	-19-
3.2 Dilution Refrigerator	-19-
3.3 Faraday force magnetometer	-22-
3.3.1 Method of measurement	-22-
3.3.2 Design and performance of the load cell	-23-
3.4 The Muon Spin Rotation (μ SR) technique	-26-
3.4.1 Experimental setup	-26-
3.4.2 The transverse field configuration	-28-
3.4.3 Data analysis	-28-
3.4.4 Muon spin rotation	-30-

4. Experimental results	-32-
4.1 Faraday force magnetometer experiment	-32-
4.1.1 One single crystal of Fe8	-32-
4.1.2 Mosaic of single crystals of Fe8	-34-
4.1.3 Analysis of the Faraday force magnetometer experiment	-35-
4.2 μ SR experiment	-37-
4.2.1 Experimental setup	-37-
4.2.2 Muons hit the silver plate - results	-38-
4.2.3 Muons hit the silver plate - analysis	-40-
4.2.4 Muons hit the sample – results	-41-
4.2.5 Muons hit the sample – analysis	-43-
5. Discussion and summary	-45-
5.1 Comparison to the Landau-Zener model and previous experiments	-45-
5.2 The difference between Fe8 to a regular magnet	-49-
5.3 Summary	-50-
Appendixes	
A - Non adiabatic transition explained by Landau and Zener	-52-
B - Measurement of capacitance	-55-
C - The force that acts on the load cell	-59-
D - Decrease in asymmetry between the sample and holder measurement	-61-
References	-63-
Hebrew Abstract	- ' -

List of figures

- 1.2.1** Structure of the molecular nanomagnet Fe8: (a) molecular view - the spin structure is schematized by the arrows [5]; (b) crystal shape - schematic view of the anisotropy axes and the crystal axes [11].
- 1.2.2** Temperature (a) and field sweeping rate (b) dependence of hysteresis loops of Fe8 molecular clusters. Resonant tunneling is evidenced by equally separated steps of $\Delta H_z \sim 0.22$ T which, at $T=360$ mK, correspond to tunnel transitions from the state $M=-10$ to $M=10-n$, with $n=0,1,2,\dots$. The resonance widths of about 0.05 T are due to mainly dipolar fields between the molecular clusters (from [11]).
- 1.2.3** Spin states of Fe8 molecules at $H = 2D/g\mu_B$ (solid line) and at zero field (dashed line).
- 1.3.1** The atomic weight of a typical memory element, as a function of time [3, 30].
- 2.2.1** Energy levels for a spin state S with easy axis magnetic anisotropy. The $+M$ levels are localized in the left side and the $-M$ levels in the right side. a) In zero field the two sides are equally populated; b) the application of a magnetic field selectively populates the right side; c) After removing the field the system returns to equilibrium (thermally) [13].
- 2.3.1** A possible "short cut" to magnetic relaxation through tunneling between thermally activated states.
- 2.4.1** Zeeman diagram of the 21 levels of the $S=10$ manifold of Fe8 as a function of the field applied along the easy axis. From the bottom to the top, the levels are labeled with quantum numbers $M=\pm 10, \pm 9, \dots, 0$. The levels cross at fields given by $\mu_0 H_z = n \cdot 0.22$ T, with $n=1,2,3,\dots$. The inset displays the detail at a level crossing where the transverse terms (terms containing S_x and/or S_y spin operators) turn the crossing into an avoided crossing. The higher the gap Δ , the stronger the tunnel rate (from [11]).
- 3.1.1** Photograph of Fe8 single crystals.

- 3.1.2** Schematic view of Fe8 single crystal and crystallographic axes - $a = 10.64\text{\AA}$, $b = 14.12\text{\AA}$, $c = 15.09\text{\AA}$, $\alpha = 89.64^\circ$ $\beta = 109.99^\circ$ $\gamma = 109.20^\circ$
- 3.2.1** Phase diagram of $^3\text{He}/^4\text{He}$.
- 3.2.2** A schematic diagram of a dilution refrigerator.
- 3.3.1** Principle of measurement. The magnetic force \mathbf{F} exerted on a sample situated in a spatially varying field is detected as a capacitance change of the parallel-plate variable capacitor, whose movable plate is suspended by elastic springs S [26].
- 3.3.2** Cross sectional view of the load cell. The movable plate is suspended by four wires of phosphor bronze. The diameter of the capacitor plates is 16mm.
- 3.3.3** The response of the load cell to weight in room temperature.
- 3.3.4** Schematic view of the load cell device, installed off-center position of a solenoid magnet in a dilution refrigerator.
- 3.4.1** Schematic illustration for a positive pion decay into a muon and a neutrino (Taken from [30]).
- 3.4.2** (a) Angular distribution of the positrons from the muon decay for various positron energies (Taken from [31]). (b) The mirror image of the muon decay. The direction of the muon-spin is reversed in the mirror so that the positrons are emitted predominantly in a direction opposite to that of the muon-spin. The violation of parity means that in our universe only the process on the left-hand side of the diagram is ever observed (taken from [32]).
- 3.4.3** Transverse field setups.
- 3.4.4** Simulated raw positron spectra in forward and backward detectors (a) for transverse field (TF) and longitudinal/zero field (ZF) geometries with the associated corrected asymmetry spectra (b). Taken from [13].
- 3.4.5** The muon polarization $\mathbf{P}(t)$ in the presence of a constant field \mathbf{B} .
- 4.1.1** The capacitance (in arbitrary units) verses the magnetic field at five different sweeping rates (in ~ 40 mK). The vertical dotted lines are in the approximate matching fields $H_m \approx n \times 2.2\text{T}$.
- 4.1.2** The capacitance verses the magnetic field ($dH/dt=0.15\text{T/min}$, $\text{Temp}=40\text{mK}$). One can see that the distance between steps is nearly constant (the arrows are of equal length).

- 4.1.3** The capacitance (in arbitrary units) verses the magnetic field in five different temperatures (constant sweeping rate of 0.15T/min, one single crystal). The vertical dotted lines are in the approximate matching fields $H_m \approx n \times 2.2T$.
- 4.1.4** The capacitance verses the magnetic field in five different sweeping rates (in ~ 40 mK, one single crystal). One can notice that the higher sweeping rates, the jump occurs in lower fields.
- 4.1.5** The height of the jump (in $\sim 0.17T$) as a function of the sweeping rate. The solid line is a guide to the eye (mosaic of single crystals).
- 4.2.1** The arrangement of the Fe8 single crystals in the experimental apparatus (from [20]).
- 4.2.2** (a) In the first experiment the muons stopped in the silver plate; (b) in the second experiment some of them stopped in the sample or the GE-varnish between the crystals.
- 4.2.3** Measurement on Fe8 using μ SR (muons hit the silver). Different intermediate fields (H_i) are leading to different muon rotation frequencies, especially between $H_i=0.2T$ ($-0.2T$) to $H_i=0.3T$ ($-0.3T$).
- 4.2.4** Measurement in an empty holder. Different intermediate fields (H_i) are leading to different muon rotation frequencies in low magnetic fields, but to similar frequencies in high fields (muons hit the silver plate).
- 4.2.5** The shift of the muon rotation frequency as a function of the intermediate field H_i , between an empty sample holder, and a holder with Fe8. Raw data of ω versus H_i is shown in the inset. The solid lines are guide to the eye (muons hit the silver).
- 4.2.6** Different intermediate fields (H_i) are leading to different muon rotation frequencies in Fe8 (a, b & c), but to similar frequencies in an empty holder (d, e & f).
- 4.2.7** The shift of the muon rotation frequency (hence the magnetic field he sense) as a function of the intermediate field H_i , between an empty sample holder, and a holder with Fe8. Raw data of ω versus H_i with, and without, Fe8 is shown in the inset (muons hit the sample). The solid line is a guide to the eye.
- 5.1.1** Field sweeping rate dependence of the effective tunnel splitting Δ measured by a Landau Zener method (a). The measured Landau-Zener tunneling probability P is

- indicated for several field sweeping rates. (b) Measured tunnel splitting Δ as a function of transverse field for $\varphi=0^\circ$ (parallel to the easy axis), and for quantum transition between $M = -10$ and $(S - n)$ [11, 20].
- 5.1.2** Schematic diagram of the probability to tunnel from $m = -10$ to $m' = 10,9$, during a three field cycle experiment with $0.2T < H_i < 0.4T$. The probability not to tunnel is given by: $(1-P_{-10,10}) \times (1-P_{-10,9})^2$.
- 5.1.3** Our μ SR results on Fe8, $(2\Delta\alpha(H_i) - \Delta\alpha_0 - \Delta\alpha_\infty) / (\Delta\alpha_\infty - \Delta\alpha_0)$, with the dotted line as a guide to the eye, and theoretical prediction (solid blue line) due to the Landau Zener model, $P_{up}(H_i) - P_{down}(H_i)$. The steps appear at the right place but not with the predicted height.
- 5.1.4** Hysteresis loops measured by Wernsdorfer in the presence of a constant transverse field, at 0.04 K. Insets: Enlargement around the field $H=0$. Notice that the sweeping rate is ten times slower for the measurements in the insets than that of the main figures. Taken from [11].
- 5.2.1** The same experiment ($1.5T \rightarrow H_i \rightarrow$ measurement in $0.005T$) has been done on SmCo (a), a regular permanent magnet with similar saturation field. There is only one plateau compare to Fe8 with 2-3 plateaus (b).
- A.1** Crossing of energy levels.
- B.1.1** Schematic diagram of a capacitor showing the direct capacitance and its associated terminal capacitances.
- B.1.2** Diagram of three terminal capacitor.
- B.2.1** Basic ratio bridge.
- B.2.2** A capacitance bridge with transformer ratio arms.
- B.3.1** Basic bridge circuit of AH2550A Capacitance Bridge.
- D.1** A demonstration that Fe8 depolarize muons immediately. The asymmetry of a hematite and glue mask (a) is very similar to mask and Fe8 (b), but different from mask and silver (c). Therefore, muons in Fe8 do not contribute asymmetry.

List of Tables

- 3.1.1 The results of chemical microanalysis of Fe8.
- 3.1.2 The results of X-ray crystallography Analysis.

Abstract

Molecular clusters of paramagnetic metal ions have been widely investigated as a model for magnetism at the nanoscale, especially for quantum effects such as the tunneling of the magnetic moment. The molecular magnet $[(C_6H_{15}N_3)_6Fe_8O_2(OH)_{12}]Br_7(H_2O)Br \cdot 8H_2O$, abbreviated Fe8, is a representative compound in which quantum tunneling of magnetization (QTM) has been observed. This molecule is particularly interesting since it exhibits 'pure' quantum tunneling of the magnetization, namely, the tunneling rate is temperature independent below $T \approx 400$ mK [1, 2].

This field was investigated intensively and became more interesting for its possible future applications. Technology today has reached a point where a single atom and a single molecule can be manipulated. This, essentially, allows reduction of the size of a magnetic memory unit from a billion atoms per bit used today [3], to a single molecule. The difficulty lies in the stability of the stored information. Spin polarization, and hence the memory stored in a single molecule, can be lost not only by thermal effects, but also via magnetic quantum tunneling without thermal assistance. As a result considerable effort is being exerted to understand the mechanism of magnetic quantum tunneling in the hope of one day preventing it. There is also an ongoing effort to make Fe8 films; once this goal is achieved there will be a need to confirm that the molecules in the films behave as the molecules in the bulk. This is not a simple task since measurements that have been used up to date such as susceptibility, specific heat, NMR, etc. need relatively large samples and cannot be applied on thin films.

The main objective of this work is devoted to the development of the muon spin rotation (μ SR) technique as a probe of QTM in Fe8 high spin molecules (HSM), since it is applicable to films [4]. We show that this technique is sensitive to the quantum nature of the molecules. We also present evidence for the quantum nature of the Fe8 single crystals using Faraday force magnetometer experiment.

As a by product of our experiment, we demonstrate the fact that Fe8 can be used as multi-bit memory. This possibility was suggested before by A. Caneschi et al. [5] but was never

demonstrated experimentally. By applying different process (three fields cycle) to the Fe₈ crystals and detecting the magnetization afterwards, we discovered that it is possible to generate clearly distinguishable muon frequencies (more than two) as a result of these processes. Therefore, with the same setup of measurement we can distinguish between the different "histories" (the process before the measurement) of the molecules. This warrants Fe₈ molecules the candidacy for a multi-bit magnetic memory (as apposed to regular memory unit which is binary).

List of Symbols and abbreviations

Symbol	Meaning
QTM	quantum tunneling of magnetization
HSM	high spin molecules
μ SR	muon spin rotation
EPR	electron paramagnetic resonance
DR	dilution refrigerator
TF	transverse field
LF	longitudinal field
ZF	zero field
J	magnetic coupling between ions inside a high spin molecule
S	quantum number of the total spin at the ground state
S_z	spin component in the z direction
\mathcal{H}	spin Hamiltonian
D	anisotropy parameter of the uniaxial term
E	anisotropy parameter of the rhombic term
k_B	Boltzmann constant, 1.38066×10^{-23} [J]/[K]
T	Temperature
\mathbf{H}	external magnetic field
H_x	the x component of the external magnetic field
H_m	matching field
\mathbf{B}	magnetic flux density
m	quantum number of the spin in the z direction
g	the spectroscopic splitting factor
μ_B	Bohr magneton, 9.274×10^{-24} [J]/[T]
H_i	intermediate field
\mathbf{M}	Magnetization
P	tunneling probability

Symbol	Meaning
ω	Frequency
\hbar	Plank's constant, $1.05457 \times 10^{-34} [\text{J}][\text{s}]$
t	Time
$\Delta_{m,m'}$	tunnel splitting
$A(t)$	asymmetry as a function of time
C	Capacitance
C_0	initial capacitance
A	area of the capacitor plates
I	moment of inertia
F	Force
δ	displacement of the capacitor plate
d	distance between the capacitor plates
ϵ_0	permittivity of vacuum, $8.85419 \times 10^{-12} [\text{F}]/[\text{m}]$
E_y	Young's modulus
γ	gyromagnetic ratio

Chapter 1

Preface

Recently, molecular nanomagnets have attracted much attention to the study of quantum mechanical phenomena occurring in macroscopic systems, owing to their identical size, well defined structure, and a well-characterized energy structure. The molecular magnet $[(C_6H_{15}N_3)_6Fe_8O_2(OH)_{12}]Br_7(H_2O)Br \cdot 8H_2O$, abbreviated Fe8, is a representative compound in which quantum tunneling of magnetization (QTM) has been observed, in the form of temperature independent recovery of magnetization below 400 mK [1].

1.1 Introduction - high spin molecules (HSM)

The molecular nanomagnet Fe8 belongs to a family called high spin molecules (HSM). HSM are molecules consisting of ions coupled by ferromagnetic or antiferromagnetic interaction; these molecules crystallize in a lattice where neighboring molecules are very well separated. At temperatures lower than the magnetic coupling J between ions inside the high spin molecule, the spins of the ions are locked, and the molecules behave like non-interacting spins. The energy difference between the ground spin state and the next excited spin state is of the order of J , therefore at low temperatures only the ground spin state S is populated. This state is $2S+1$ times degenerate in first order approximation. However at even lower temperatures the degeneracy can be removed by additional magneto-crystalline anisotropic interactions such as the uniaxial term DS_z^2 , or rhombic term $E(S_x^2 + S_y^2)$, etc. When the temperature is high enough transitions between different spin states of the molecules are thermally activated, but when the temperature is much lower than the energy difference between spin states, the transitions between them are only possible through the tunneling.

1.2 Quantum tunneling of the magnetization (QTM) in Fe8

A Fe8 molecular cluster was synthesized first in 1984 [6] and it consists of eight Fe^{3+} ions ($s = 5/2$), as shown in Fig.1.2.1a. The magnitude of magnetic interactions between the spins of the Fe^{3+} ions in the molecule is between 20 to 170K [7], and the magnetic

interactions between the molecules are negligibly small. The magnetic properties of this compound at low temperatures have been described by a simple spin model with total spin of $S = 10$ in which six spins are parallel to each other and the remaining two spins are anti-parallel to the other spins (see Fig. 1.2.1a; this model was experimentally confirmed by a polarized neutron-diffraction experiment [8]). The experimental results of the magnetization curves at low temperatures show large anisotropy that is dependent on the orientation of the external magnetic field with respect to the crystal axis [8]. The magnetization is preferentially oriented parallel to an axis called the "easy axis", which in Fe8 is oriented with an azimuthal angle of 16° from the a -axis in the ab -plane and an inclinational angle of 0.7° from the ab -plane as can be seen in Fig 1.2.1b.

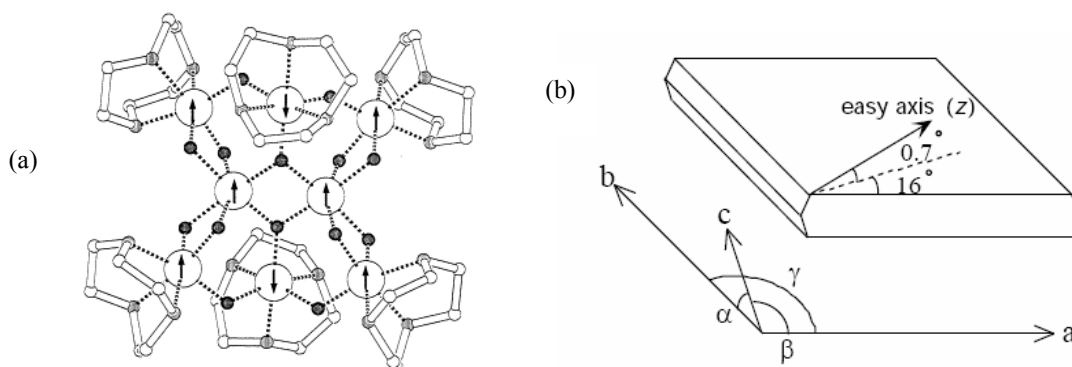


Figure 1.2.1: Structure of the molecular nanomagnet Fe8: (a) molecular view - the spin structure is schematized by the arrows [5]; (b) crystal shape - schematic view of the anisotropy axes and the crystal axes [11].

Fe8 is ideal for investigating quantum effects that affect the magnetization dynamics. There are several reasons for that: The biaxial anisotropy has been carefully measured [7], and a reasonably large transverse term promotes tunneling effects; In addition, the experimentally observed barrier (between spin up and down, Fig. 1.2.3) is ~ 24 K [7] which is not too high, and apparently the samples contain only one crystallographic phase [5]. The net result is that the relaxation of the magnetization becomes temperature independent below 0.4 K suggesting that a pure tunneling regime is attained [1]. In this regime the relaxation of the magnetization near a resonance is of the order of hours and experiments can therefore measure a significant part of the magnetization decay.

The magnetization of Fe₈ molecules as a function of external field is presented in Fig 1.2.2, exhibiting hysteresis and steps at well defined field values [11]. On the left side (Fig 1.2.2a) one can see the dependence on the temperature of the 'staircase' structure above 0.4mK and in constant sweep rate. On the right side (Fig. 1.2.2b), five curves taken at 40 mK are shown, with five different ramping rates. The steps for all ramping rates occur at the same field values, but the size of the step is different for different ramping rates.

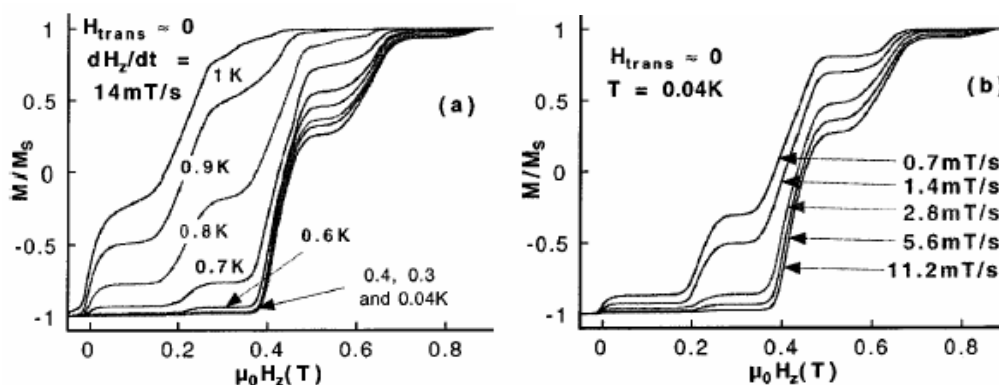


Figure 1.2.2: Temperature (a) and field sweeping rate (b) dependence of hysteresis loops of Fe₈ molecular clusters. Resonant tunneling is evidenced by equally separated steps of $\Delta H_z \sim 0.22$ T which, at $T=360$ mK, correspond to tunnel transitions from the state $M=-10$ to $M=10-n$, with $n=0,1,2,\dots$. The resonance widths are about 0.05 T, mainly due to dipolar fields between the molecular clusters (from [11]).

When sweeping the magnetic field applied along the easy axis of a Fe₈ sample (from high negative to positive fields), and at very low temperatures, one obtains a considerable decrease in the relaxation time of the magnetization for certain magnetic fields [1, 11], corresponding to those in which the steps are observed in the hysteresis loop. This decrease means that at these fields equilibrium is reached faster.

This behavior is attributed to quantum tunneling of the magnetization (QTM) within a simple model of a double well with 10 spin up states corresponding to $m = +10; +9; \dots; +1$ and 10 spin down states corresponding to $m = -10; -9; \dots; -1$ (Fig. 1.2.3). The enhancement of the relaxation rate, as well as the steps in the hysteresis loop, can be understood within this simple model (more details will be given in chapter 2).

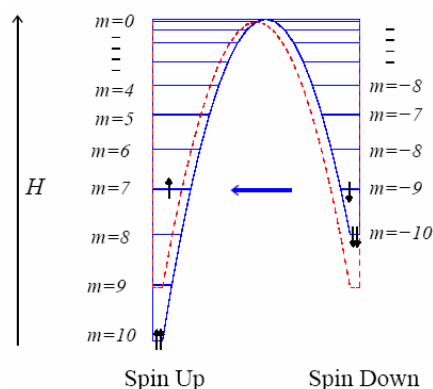


Figure 1.2.3: Spin states in Fe8 molecule at $H = 2D/g\mu_B$ (solid line) and at zero field (dashed line).

1.3 Motivation for this work

QTM has great technological importance because nano-magnets can be utilized in the industry for recording, information transmission, and computing [12]. Fig. 1.3.1 shows that magnetic computer memory elements have decreased exponentially in size over the last 40 years. At present, computers as well as magnetic tapes use elements which behave classically and are stable over long periods of time. This stability over decades exists because the size of these elements is big, and the energy barrier between two states of the element usually exceeds $100 k_B T$ even at room temperature. However, in the next few years, the necessity to enhance computer performance will challenge technology to reach the limits of size for such elements, with 10^2 - 10^5 atoms per memory element. Hence, quantum effects will be important, and we will eyewitness the transition from the classical to the quantum world. The hysteresis curves of Fe8 have presented one of the most elegant demonstration of QTM but they also make it more appealing for technological applications as it represent a multi- rather than a bi-stable single molecule memory unit [5].

There is also an ongoing effort to make Fe8 films. Once this goal is achieved there will be a need to confirm that the molecules in the films behave as the molecules in the bulk. This is not a simple task since measurements that have been used up to date such as susceptibility, specific heat, NMR, etc. can measure only relatively large samples and

cannot be applied on thin films. There are only a few techniques that can measure hysteresis loops in thin films, and one of them is MuSR- Muon Spin Relaxation/Rotation [4]. The main purpose of this work is to show that measuring QTM in Fe8 single crystals is possible by using the MuSR technique. As a by product, we also demonstrate that Fe8 can serve as a multi bit magnetic memory.

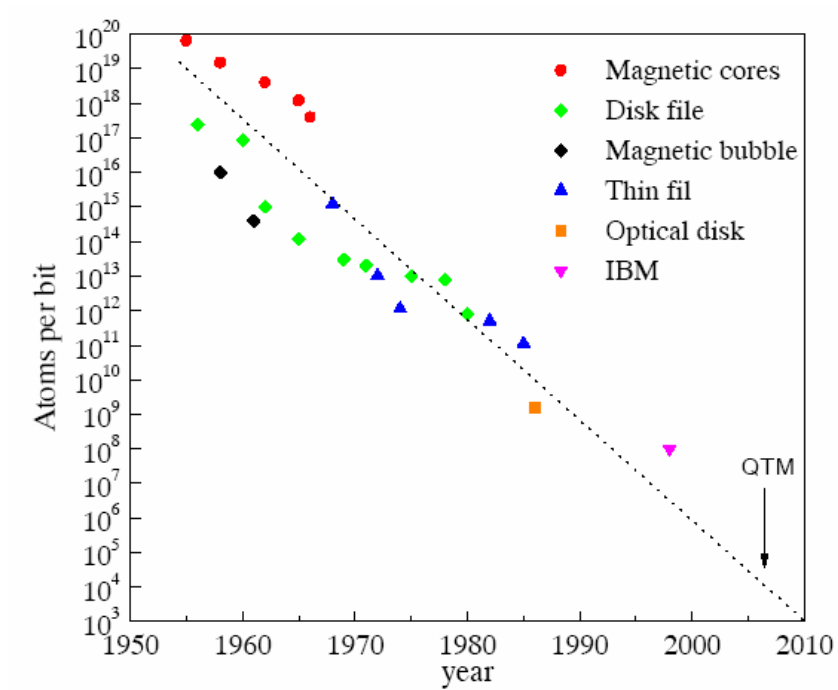


Figure 1.3.1: The atomic weight of a typical memory element, as a function of time [3, 13].

Chapter 2

Quantum Tunneling In High Spin Molecules

There is no theoretical limitation that in principle forbids observing quantum effects in larger particles, although it is known that the tunneling probability scales exponentially with the barrier height and the particle mass. Therefore tunneling is expected to be most observable in small particles and at low temperatures.

2.1 Tunneling between degenerate states

The simplest model is that of a positive (up) and negative (down) spin states with an energy barrier between them. When these states are coupled, spin up and down stop to be the eigenstates of the system, and the ground state is the anti-symmetric superposition of the two states, namely, $\psi_{as} = (\psi_{down} - \psi_{up})/2$. This state is separated by a tunnel splitting energy Δ from the symmetric wave function $\psi_s = (\psi_{down} + \psi_{up})/2$. This can be more clear by an example of a system with spin $S=1/2$. Let us take a simple Hamiltonian:

$$\mathcal{H} = DS_z^2 + g\mu_B(h_x S_x - h_z S_z) = \begin{pmatrix} -D/4 - g\mu_B h_z & g\mu_B h_x / 2 \\ g\mu_B h_x / 2 & -D/4 + g\mu_B h_z \end{pmatrix} \quad (2.1.1)$$

where D is a negative parameter, h_z (h_x) is the magnetic field strength in the \hat{z} (\hat{x}) direction, $g=2$ and μ_B is Bohr magneton. When $h_z=h_x=0$, we get two degenerate eigenstates, spin “up”- $\begin{pmatrix} 1 \\ 0 \end{pmatrix}$ and spin “down”- $\begin{pmatrix} 0 \\ 1 \end{pmatrix}$ with the same $Energy = -D/4$.

However, when $h_x \neq 0$, the two states are coupled and the eigenvalues and the eigenvectors of the Hamiltonian are the symmetric and anti-symmetric superpositions ($h_z \neq 0$):

$$\begin{aligned} \frac{1}{\sqrt{2}} \begin{pmatrix} 1 \\ 1 \end{pmatrix} &\rightarrow Energy_s = -D/4 + g\mu_B \sqrt{h_x^2 + h_z^2}, \\ \frac{1}{\sqrt{2}} \begin{pmatrix} 1 \\ -1 \end{pmatrix} &\rightarrow Energy_{as} = -D/4 - g\mu_B \sqrt{h_x^2 + h_z^2} \end{aligned} \quad (2.1.2)$$

These energies as a function of h_z are two hyperboles with a minimal gap of $\Delta_0 = g\mu_B h_x$.

If the initial state of the system is “up”, which is not an eigenstate anymore, there is some probability that tunneling will occur between “up” and “down” states:

$$P(t, h_z) = \left| \langle up | \exp\left(\frac{-i\mathcal{H}t}{\hbar}\right) | down \rangle \right|^2 = \frac{h_x^2}{h_x^2 + h_z^2} \left[\frac{1}{2} - \frac{1}{2} \cos\left(\frac{g\mu_B \sqrt{h_x^2 + h_z^2}}{\hbar} t\right) \right]. \quad (2.1.3)$$

From this equation we can learn that the probability decreases when h_z increases, but when $h_z = 0$ the system will oscillate between the two states at a frequency of $g\mu_B h_x / \hbar = \Delta_0 / \hbar$. In practice, due to the environment these oscillations are not observed and only tunneling between one state to the other can be detected. The smaller Δ_0 , which is called the “tunnel splitting”, the smaller the possibility of observing tunneling.

2.2 \mathcal{H}_0 and Magnetic Relaxation

Let us consider the Fe8 system with a well defined ground spin state, characterized by a large value of $S=10$. The unperturbed Hamiltonian includes the effect of an external magnetic field parallel to the easy axis of the cluster and of its axial splitting as a result of crystal-field effects. At this level of approximation only second-order crystal-field effects will be included. Therefore, the \mathcal{H}_0 Hamiltonian can be written as [14, 15]:

$$\mathcal{H}_0 = DS_z^2 + g\mu_B H_z S_z \quad (2.2.1)$$

where D is a negative constant for the system of interest and H_z is the magnetic field strength in the \hat{z} direction. In Fe8, the value of D/k_B is reported to be -0.275 K and -0.292 K by electron paramagnetic resonance (EPR) and neutron spectroscopy, respectively [2, 8]. The energies of the spin levels corresponding to \mathcal{H}_0 can be calculated as given by:

$$E(M_s) = DM_s^2 + g\mu_B M_s H_z \quad (2.2.2)$$

where $-S \leq M_s \leq S$. The energy levels can be plotted as shown in Fig. 2.2.1a. When no external field is applied all the levels are degenerate pairs, except $M_s = 0$. Since D is negative the $M_s = \pm S$ levels will lie lowest. In Fig. 2.2.1 the states with positive M_s are plotted in one side of the barrier, and those with negative M_s in the other. Such a system is characterized by magnetic anisotropy along the easy axis, which means that the magnetization is preferentially oriented parallel to the \hat{z} axis.

When a field is applied parallel to the \hat{z} axis the levels characterized by a positive M_S correspond to a projection of the magnetization anti-parallel to the field, while those with negative M_S correspond to magnetization parallel to the applied external field (Fig. 2.2.1b). The system can be prepared in a magnetized state by applying a magnetic field parallel to the \hat{z} axis. If the temperature T is low and the field H_z large, the $M_S = -10$ state will be the only one populated and the magnetization will reach the saturation value. When the field is removed the system must go back to thermal equilibrium (relaxation – see Fig. 2.2.1c). This means that at equilibrium half of the molecules must be in the $M_S = -10$ and half in the $M_S = 10$ state, with no resulting net magnetization.

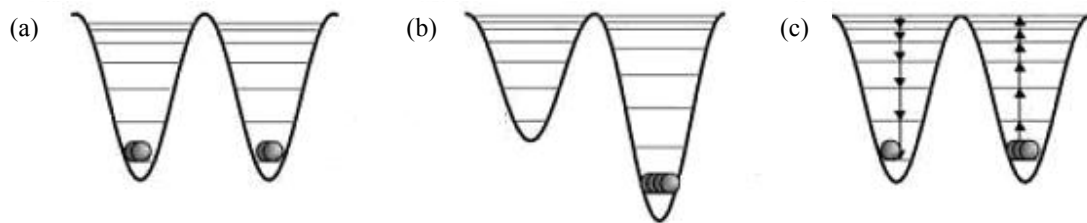


Figure 2.2.1: Energy levels for a spin state S with easy axis magnetic anisotropy. The $+M$ levels are localized in the left side and the $-M$ levels in the right side. a) In zero field the two states are equally populated; b) the application of a magnetic field selectively populates the right side; c) After removing the field the system returns to equilibrium (thermally).

2.3 The tunneling process

At low temperatures only the degenerate $M_S = \pm 10$ levels will be populated, but, as long as $\mathcal{H} = \mathcal{H}_0$ [Eq. 2.2.1] the two states are orthogonal to each other, and there is no possibility of tunneling. In principle, since the two states are degenerate, all their linear combinations will be eigenfunctions of the system. But to observe tunneling the two functions must be admixed by some suitable perturbation. Therefore, if we want to observe tunneling we must introduce the perturbation Hamiltonian \mathcal{H}_1 that allows the mixing of the two states. The tunneling process involving otherwise degenerate levels is named resonant tunneling [2].

From a physical point of view it is possible to think of a distortion which removes the axial symmetry that we have assumed for \mathcal{H}_0 . This situation corresponds to the

introduction of anisotropy in the x-y plane, or, as it is often called, a transverse anisotropy. A convenient form for the \mathcal{H}_1 Hamiltonian is:

$$\mathcal{H}_1 = E \cdot (S_x^2 - S_y^2) \quad (2.3.1)$$

where E is a parameter, which, without loss of generality [14] is limited to be $0 \leq E/D \leq 1/3$. In Fe8, E/k_B is reported to be -0.046 K and -0.047 K by EPR and neutron spectroscopy, respectively [2, 16], so $E/D \sim 0.16$. Therefore the resulting Hamiltonian $\mathcal{H} = \mathcal{H}_0 + \mathcal{H}_1$ is given by:

$$\mathcal{H} = DS_z^2 + g\mu_B H_z S_z + E \cdot (S_x^2 - S_y^2) \quad (2.3.2)$$

The Hamiltonian \mathcal{H}_1 does not commute with \mathcal{H}_0 , therefore the eigenstates of the full Hamiltonian $\mathcal{H} = \mathcal{H}_0 + \mathcal{H}_1$ are an admixture of $|M_S\rangle$ states, also with different sign of M_S . The wavefunction is therefore partially delocalized on both wells and this may give rise to tunneling, which may occur not only between the lowest-lying states $M_S = \pm S$, but also between pairs of degenerate excited states. This phenomenon is called the phonon-assisted (or thermally activated) tunneling mechanism, as phonons need to be adsorbed to populate the higher M_S states involved in the tunneling process. This mechanism is very important at intermediate temperature because the tunneling frequency is expected to increase on decreasing $|M_S|$. Therefore it offers a shortcut for the relaxation mechanism of the molecules. In principle a molecule may not need to go over the maximum of the barrier even at relatively high temperatures, but may find a shortcut and tunnel (Fig. 2.3.1)

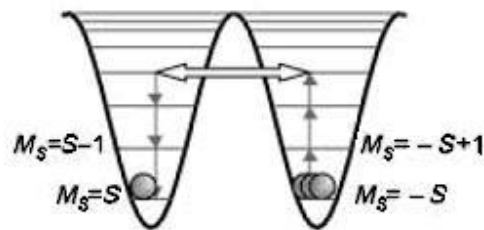


Figure 2.3.1: A possible "short cut" to magnetic relaxation through tunneling between thermally activated states [14].

2.4 Tunneling in non-zero external magnetic fields

If a magnetic field is applied parallel to the \hat{z} axis the energies of the M_S levels change rapidly, with a slope equal to $M_S \cdot g \cdot \mu_B$ (Eq. 2.2.2), it is apparent that the pairs of $\pm M_S$ levels will no longer be degenerate, and the conditions for tunneling will be lost. However, since the energy of the $M_S = S$ level increases and that of the $M_S = -S+n$ level decreases, they will have to meet somewhere, restoring the conditions for resonant tunneling. The field, at which this occurs, for axial symmetry and considering only second-order anisotropy terms, is given by the equation:

$$H_m(n) = \frac{nD}{g\mu_B} = n \times 0.22T \quad (2.4.1)$$

here H_m is called “matching” field. It is easy to show that if only the parameter D is included, all the $+M_S$ levels will cross the $-M_S$ levels at the same field. This is no longer true if higher-order terms are included.

The energy levels appropriate to the Hamiltonian, which include the transverse anisotropy term (Eq. (2.3.1)), can be calculated by diagonalizing the 21×21 matrix of the $2S+1$ states ($S=10$). The results are plotted in Fig. 2.4.1, which shows the energy levels in the presence of an applied magnetic field parallel to the \hat{z} axis, the so-called easy axis.

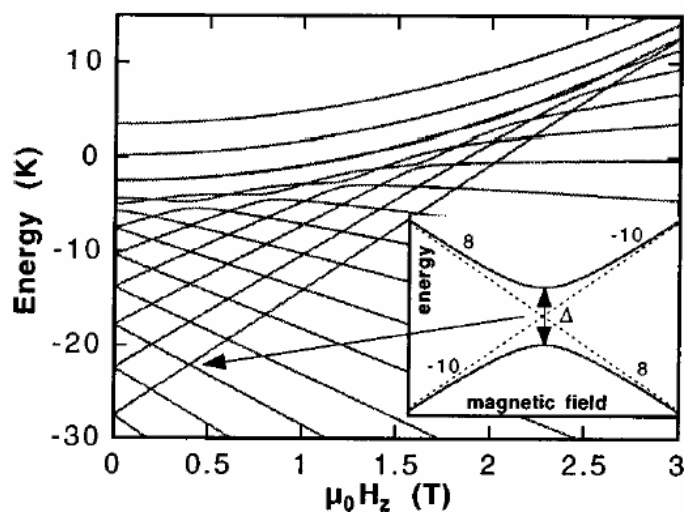


Figure 2.4.1: Zeeman diagram of the 21 levels of the $S=10$ manifold of Fe8 as a function of the field applied along the easy axis. From the bottom to the top, the levels are labeled with quantum numbers $M=\pm 10, \pm 9, \dots, 0$. The inset displays in detail a two level crossing where the transverse terms (terms containing S_x and/or S_y spin operators) turn the crossing into an avoided crossing (from [11]).

As shown in the inset of Fig. 2.4.1, the two level crossing turn into an avoided crossing with a gap Δ which is the tunnel splitting. Due to Chudnovsky & Garanin [17], this tunnel splitting Δ that can be calculated for the ground state splitting ($m=-S, m'=-m-k=-S-k$) by:

$$\Delta_k = g_k \left(\frac{E}{8D} \right)^{S-k/2} \quad (2.4.2)$$

where:

$$g_k = \frac{8D}{[(S-k/2-1)!]^2} \sqrt{\frac{(2s-k)!(2S)!}{k!}}. \quad (2.4.3)$$

2.5 Landau Zener method

The non-adiabatic transition between the two states in a two level system has first been discussed by Landau, Zener and also Stückelberg [18, 19, 20]. The original work by Zener concentrated on the electronic states of a biatomic molecule, while Landau and Stückelberg considered two atoms which undergo a scattering process.

The Landau–Zener model has been applied to spin tunneling in Fe8 nano-particles and clusters [14, 11, 21, 22, 23]. The tunneling probability P when sweeping the longitudinal field H_z at a constant rate over an avoided energy level crossing (inset in Fig. 2.4.1) is given by:

$$P_{m,m'} = 1 - \exp \left[- \frac{\pi \Delta_{m,m'}^2}{4 \hbar g \mu_B |m - m'| S dH/dt} \right] \quad (2.5.1)$$

Here, $\Delta_{m,m'}$ is the tunnel splitting between m and m' , which are the quantum numbers of the avoided level crossing; dH_z/dt is the constant field sweeping rates; $g = 2$; μ_B is the Bohr magneton, and \hbar is Planck's constant (see also Appendix A).

Let us start at a large negative magnetic field H_z . At very low temperature, all molecules are in the $m = -10$ ground state. When the applied field H_z is ramped down to zero, all molecules will stay in the $m = -10$ ground state. When ramping the field over the $\Delta_{-10,10}$ region at $H_z \approx 0$, there is a Landau–Zener tunneling probability $P_{-10,10}$ to tunnel from the $m = -10$ to the $m = 10$ state. $P_{-10,10}$ depends on the sweeping rate (Eq. 2.5.1), i.e. the slower the sweeping rate, the larger $P_{-10,10}$. When the field H_z is now further increased, there is a

remaining fraction of molecules in the $m = -10$ state which becomes a metastable state. The next chance to escape from this state is when the field reaches the $\Delta_{10,9}$ -region. There is a Landau-Zener tunneling probability $P_{-10,9}$ to tunnel from the $m = -10$ to the $m = 9$ state. As $m = 9$ is an excited state, the molecules in this state relaxes quickly to the $m = 10$ state by emitting a phonon. An analogous procedure happens when the applied field reaches the $\Delta_{-10,10-n}$ - region ($n = 2, 3, \dots$) until all molecules are in the $m = 10$ ground state, *i.e.* the magnetization of all molecules is reversed.

Chapter 3

Experimental methods

3.1 Sample preparation

Single crystals of $[(C_6H_{15}N_3)_6Fe_8O_2(OH)_{12}]Br_7(H_2O)Br \cdot 8H_2O$, were synthesized by the following steps:

- **Synthesis of $(C_6H_{15}N_3)FeCl_3$** [24]

1.6 ml of ethanol with 0.2g 1,4,7-triazacyclononane (tacn) is added to a solution of $FeCl_3 \cdot 6H_2O$ (0.45 g) in ethanol (12.8 ml). The resulting bright yellow precipitate of $(tacn)FeCl_3$ is filtered off, washed with ethanol, and air-dried (0.35 g).

- **Synthesis of Fe8** [6]

0.35g of $(tacn)FeCl_3$ was dissolved in 28 ml H_2O and 2.8 ml pyridine, while rotating the entire solution for about 15 min. Then 7g of NaBr was added to the solution. In contrary to Wieghardt et. al. [6], nothing happened after 24 hours. After two-three weeks, brown crystals of Fe8, $[(C_6H_{15}N_3)_6Fe_8O_2(OH)_{12}]Br_7(H_2O)Br \cdot 8H_2O$, separated out. The maximum size of the synthesized single crystals are about $3 \times 2 \times 1 \text{ mm}^3$. It is possible to add to the solution (after the NaBr) one single crystal of Fe8 and then one can obtain a bigger single crystal ($8 \times 6 \times 1.5 \text{ mm}^3$).

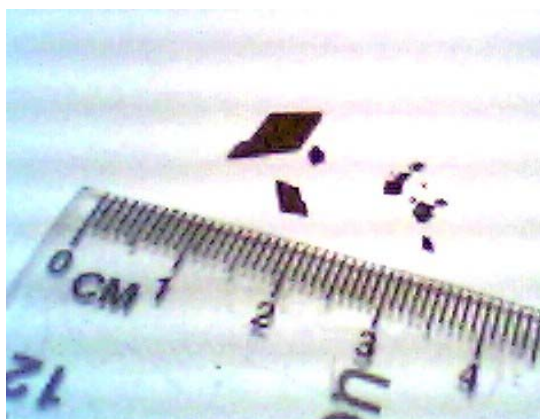


Figure 3.1.1: Photograph of Fe8 single crystals.

Preparing the samples under high magnetic fields (up to 8 Tesla) did not change the outcoming crystals.

3.1.1 Chemical analysis

The sample was sent to the microanalysis lab (Hebrew University) for chemical analysis.

The results of the analysis were:

Element	Carbon (C)	Hydrogen (H)	Nitrogen (N)	Brome (Br)
% calculated	20.6	4.8	12	28.41
% found	18.68	5.19	10.64	28.14

Table 3.1.1: The results of chemical microanalysis of Fe8

3.1.2 X-ray crystallography analysis

A small fragment from a large crystal was mounted on the Nonius Kappa CCD diffractometer using $Mok\alpha$ radiation and ambient temp. Cell parameters were obtained from ten frames as follows:

$a = 10.64\text{\AA}$, $b = 14.12\text{\AA}$, $c = 15.09\text{\AA}$, $\alpha = 89.64^\circ$ $\beta = 70.01^\circ$ $\gamma = 70.80^\circ$. By shift of origin by one translation along a axis, the following cell parameters are obtained: $a = 10.64\text{\AA}$, $b = 14.12\text{\AA}$, $c = 15.09\text{\AA}$, $\alpha = 89.64^\circ$ $\beta = 109.99^\circ$ $\gamma = 109.20^\circ$. These parameters are rather close to those given by Wiegardt et al. at 243 K [6] as shown the following table:

Crystal parameters	a [Å]	b [Å]	c [Å]	α	β	γ
Wiegardt et al.[6] (243K)	10.522	14.05	15.00	89.90°	109.65°	109.27°
X-ray crystallography Analysis (27°C)	10.64	14.12	15.09	89.64°	109.99°	109.20°

Table 3.1.2: The results of X-ray crystallography analysis

A schematic view of Fe8 single crystal and its crystallographic axes are shown in Fig. 3.1.2.

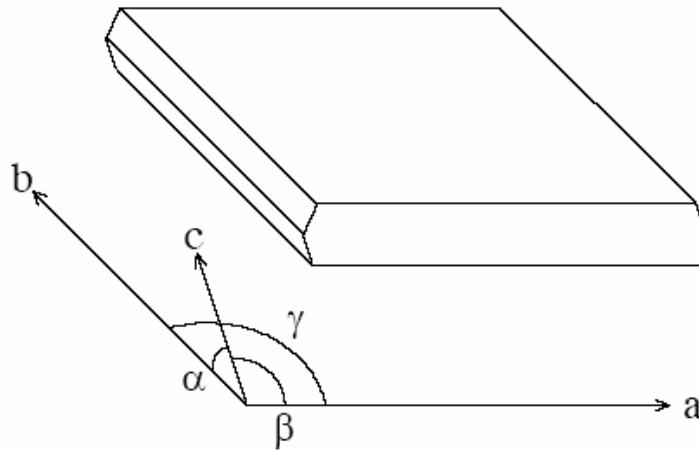


Figure 3.1.2: Schematic view of Fe8 single crystal and crystallographic axes -
 $a = 10.64\text{\AA}$, $b = 14.12\text{\AA}$, $c = 15.09\text{\AA}$, $\alpha = 89.64^\circ$ $\beta = 109.99^\circ$ $\gamma = 109.20^\circ$.

3.2 Dilution Refrigerator

The ^3He - ^4He dilution refrigerator (DR) was used for all the measurements at the sub-Kelvin temperature range. In the Faraday force magnetometer experiment, a first time operated DR was used.

The principle of operation of the DR was originally proposed by H. London in 1962 [25]. When a mixture of the two isotopes of helium is cooled below a critical temperature, it separates into two phases as shown in Fig. 3.2.1. The higher (or lighter) "concentrated phase" is rich in ^3He and the heavier "dilute phase" is rich in ^4He . The concentration of ^3He in each phase depends upon the temperature. Since the enthalpy (the sum of the internal heat in a system and the product of its volume and pressure) of the ^3He in the two phases is different, it is possible to cool the system by "evaporating" the ^3He from the concentrated phase into the dilute phase. Although the properties of the liquids in the DR are described by quantum mechanics, it is possible to understand the cooling process in a classical way: let's regard the concentrated phase of the mixture as liquid ^3He , and the dilute phase as ^3He 'gas' which moves through the liquid ^4He without interaction. This 'gas' is formed in the mixing chamber at the phase boundary. This process continues to work even at the lowest temperatures because the equilibrium concentration of ^3He in the dilute phase is still finite, even as the temperature approaches absolute zero.

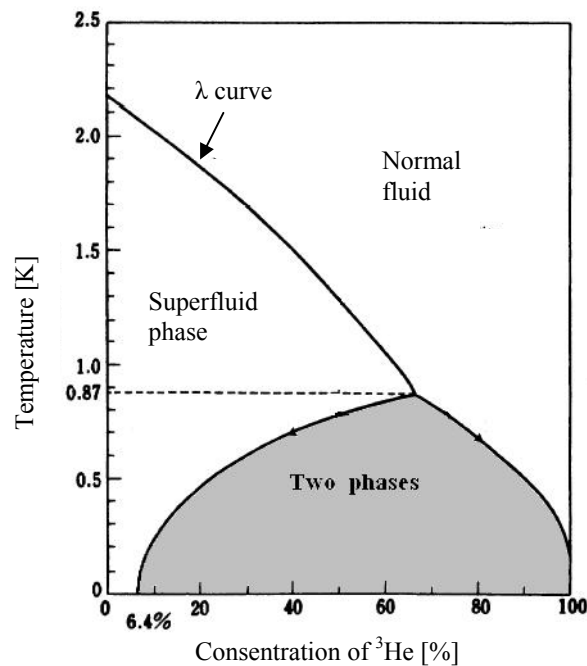


Figure 3.2.1: Phase diagram of $^3\text{He}/^4\text{He}$.

A schematic diagram of a DR is shown in Fig. 3.2.2. When the refrigerator is started the 1K pot is used to condense the $^3\text{He}/^4\text{He}$ mixture into the dilution unit. It is not intended to cool the mixture enough to set up the phase boundary but only to cool it to 1.2K. The still is the first part of the fridge to cool below 1.2 K. It cools the incoming ^3He before it enters the heat exchangers and the mixing chamber, and phase separation typically occurs after a few minutes (below 0.87 K). If the ^3He concentration in the mixture is good, the phase boundary is inside the mixing chamber, and the liquid surface is in the still.

^3He is pumped away from the liquid surface in the still, which is typically maintained at a temperature of 0.6 to 0.7 K. At this temperature the vapor pressure of ^3He is about 1000 times higher than that of ^4He , so ^3He evaporates preferentially. A small amount of heat is supplied to the still to promote the required flow. The concentration of ^3He in the dilute phase in the still therefore becomes lower than it is in the mixing chamber, and the osmotic pressure difference drives a flow of ^3He to the still. The ^3He leaving the mixing chamber is used to cool the returning flow of concentrated ^3He in a series of heat exchangers (sintered silver heat exchangers are used to decrease the thermal boundary resistance between the liquid and the solid walls).

The room temperature vacuum pumping system is used to remove ^3He from the still, and compress it to a pressure of a few hundred millibars.

The experimental apparatus is mounted on or inside the mixing chamber, ensuring that it is in good thermal contact with the diluted phase.

n

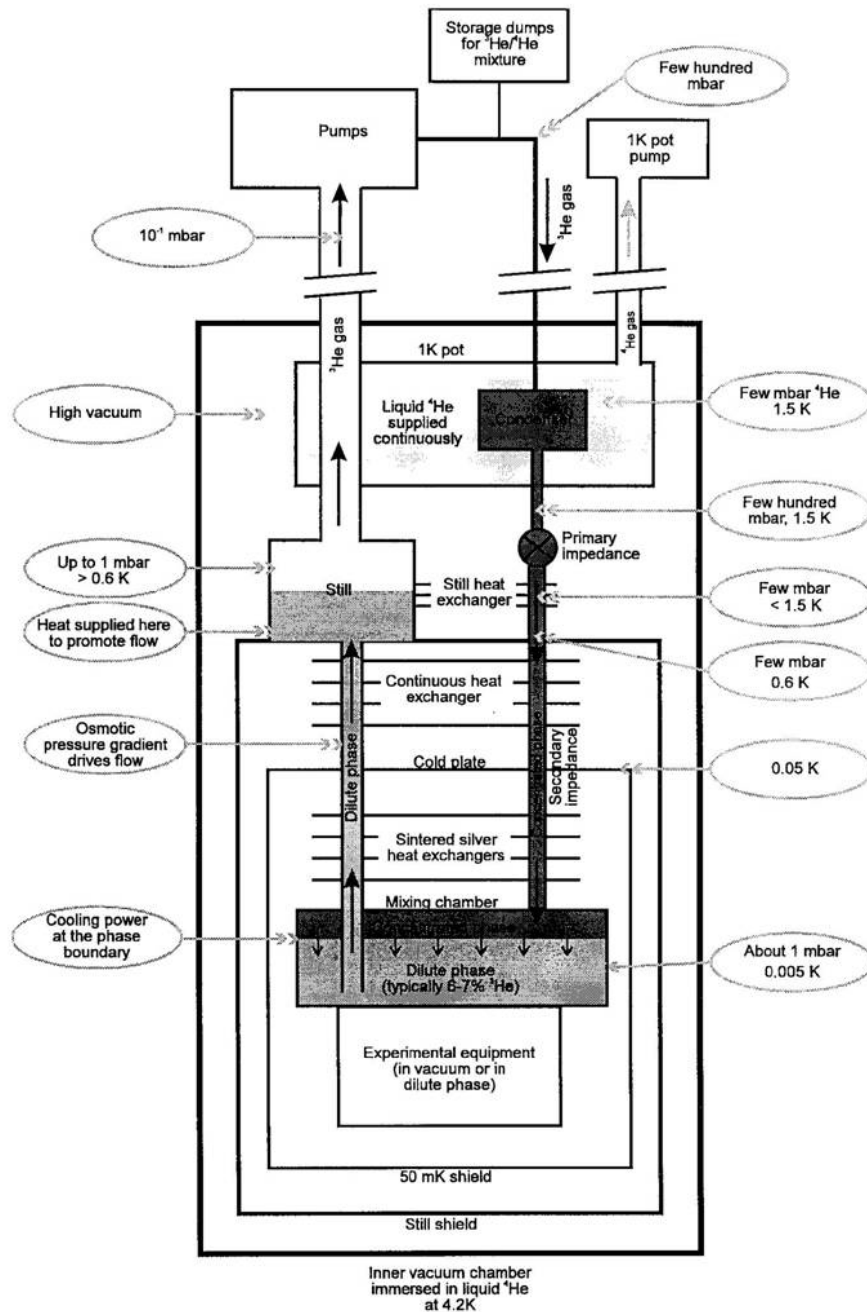


Figure 3.2.2: Schematic diagram of a dilution refrigerator [26].

3.3 Faraday force magnetometer

A Faraday force magnetometer was designed for magnetization measurement at very low temperatures by Sakakibara et al [27]. The magnetic force acting on a specimen located in the inner vacuum chamber (IVC) of a dilution refrigerator (DR) is detected by a load sensing variable capacitor.

This method has been chosen because it fits magnetic measurements in high fields and in sub-Kelvin temperatures. Other commonly used methods are (I) vibrating sample inside a coil and (II) field modulation techniques [28]. In (I) one must move the sample inside a pick up coil to drive a time varying magnetic flux. This action produces heat and warms up the sample, which becomes a serious problem at very low temperatures. On the other hand, in the field modulation (ac) method (II) one measures the differential susceptibility as a function of the applied field. Even in this method, however, heating by the time-varying modulation field may not always be negligible for metallic specimens. Moreover, there is difficulty in its application to irreversible phenomena with hysteresis in the magnetization [27]. Another reason for preferring the Faraday force magnetometer on other methods is that it could be done with no metallic parts near the sample (no coils). This is important because in the future we would like to measure the influence of RF (radio frequency) on the magnetization of the sample.

3.3.1 Method of measurement

The principle of measurement is schematically shown in Fig 3.3.1. A sample of magnetization \mathbf{M} is mounted on a small load-sensing device (\equiv load cell) made of parallel plate variable capacitor, whose movable plate is suspended by elastic springs. When the sample is subjected to a spatially varying magnetic field \mathbf{B} , it will experience a force [28]

$$\mathbf{F} = (\mathbf{M} \cdot \nabla)\mathbf{B} \quad (3.3.1)$$

If \mathbf{F} is directed perpendicular to the plates, the movable plate will then be pushed until the restoring force of the springs balances \mathbf{F} . Within an elastic deformation of the springs, the displacement of the plate is proportional to \mathbf{F} and can be detected as a capacitance change ΔC .

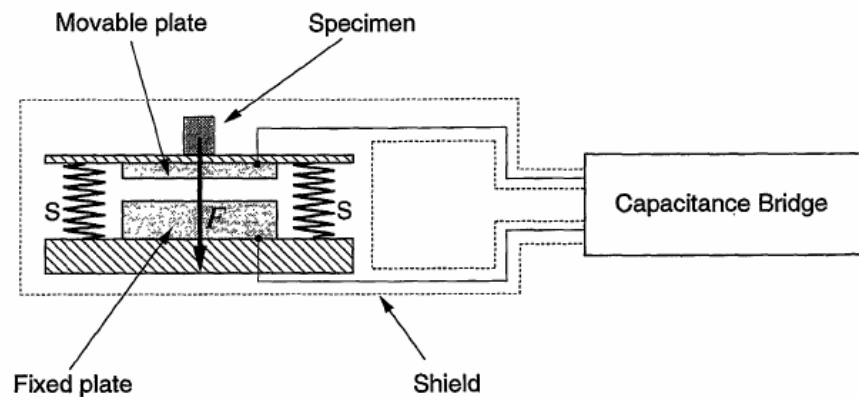


Figure 3.3.1: Principle of measurement. The magnetic force F exerted on a sample situated in a spatially varying field is detected as a capacitance change of the parallel-plate variable capacitor, whose movable plate is suspended by elastic springs S [27].

3.3.2 Design and performance of the load cell

The load cell is shown in Fig. 3.3.2. The movable plate, on which the sample is mounted, is made of epoxy (stycast #1266), with its metallized surface facing down toward the fixed plate. The diameter of the two plates is 16mm and the unloaded capacitance with a gap of $d = 0.4\text{mm}$ is $C = \epsilon_0 A/d \approx 5\text{pF}$ (where A is the area of the plate and ϵ_0 is the permittivity of vacuum). The movable plate is attached to two pairs of orthogonal crossed wires (0.2mm diameter) of phosphor bronze, strung with a tension of $\sim 0.5\text{N}$. The static plate was mounted on an epoxy screw, for adjusting the initial capacity (by adjusting the initial gap between the capacitor plates).

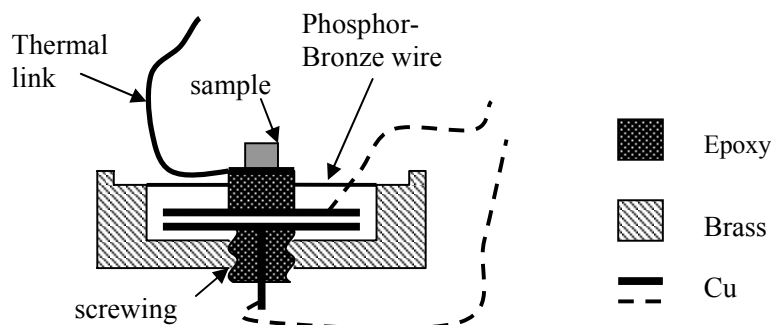


Figure 3.3.2: Cross sectional view of the load cell. The movable plate is suspended by four wires of phosphor bronze. The diameter of the capacitor plates is 16mm.

The displacement δ of a capacitor plate caused by a force F_z can be estimated using the formula [27]:

$$\delta / F_z = L^3 / 192nE_y \cdot I \quad (3.3.2)$$

where n and L are the number and the effective length of the wires (respectively), E_y is Young's modulus and I is the moment of inertia ($I = \pi D^4 / 64$) of the wire with a diameter D . From the actual values ($L=10\text{mm}$, $D=0.2\text{mm}$, $E_y \sim 1 \times 10^{10} \text{ N/m}^2$), the response of the load cell can be estimated to be $\delta / F_z \sim 0.2\text{mm} / \text{N}$, or when $C_0 \sim 5\text{pF}$: $\Delta C / F_z \sim 30\text{pF} / \text{N}$ (It is noted that ΔC is not linear with respect to force, especially above $\Delta C / C_0 \sim 0.1$).

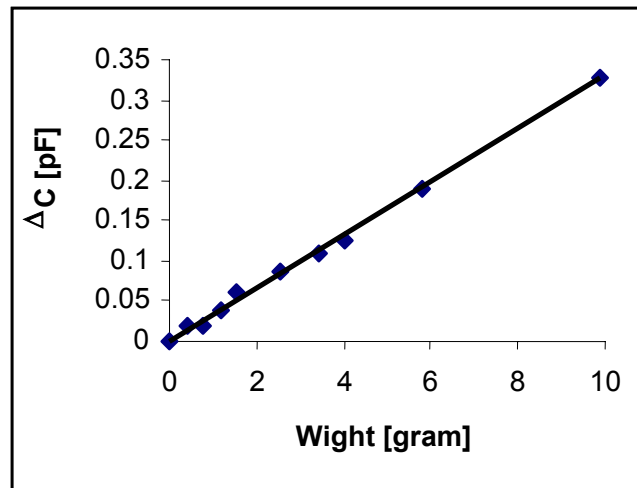


Figure 3.3.3: The response of the load cell to weight in room temperature.

To demonstrate the performance of the load cell, the response to weight in room temperature is shown in Fig. 3.3.3. The capacitance of the cell has been monitored by the three-terminal method (Appendix B) with an auto-balance digital capacitance bridge. The unloaded capacitance C_0 was 5.5pF. Neglecting edge effects of the capacitor, ΔC can be transformed to the displacement δ of the plate by the simple formula:

$$\delta = \varepsilon_0 A (C_0^{-1} - C^{-1}) \quad (3.3.3)$$

where A denotes the area of the plates, ε_0 is the permittivity of vacuum and $C = C_0 + \Delta C$.

The load response δ / F_z of the cell becomes 0.18 mm/N at room temperature (this is in

reasonable agreement with the estimated response of the load cell which was numerically estimated as $\delta / F_z \sim 0.2 \text{ mm} / \text{N}$).

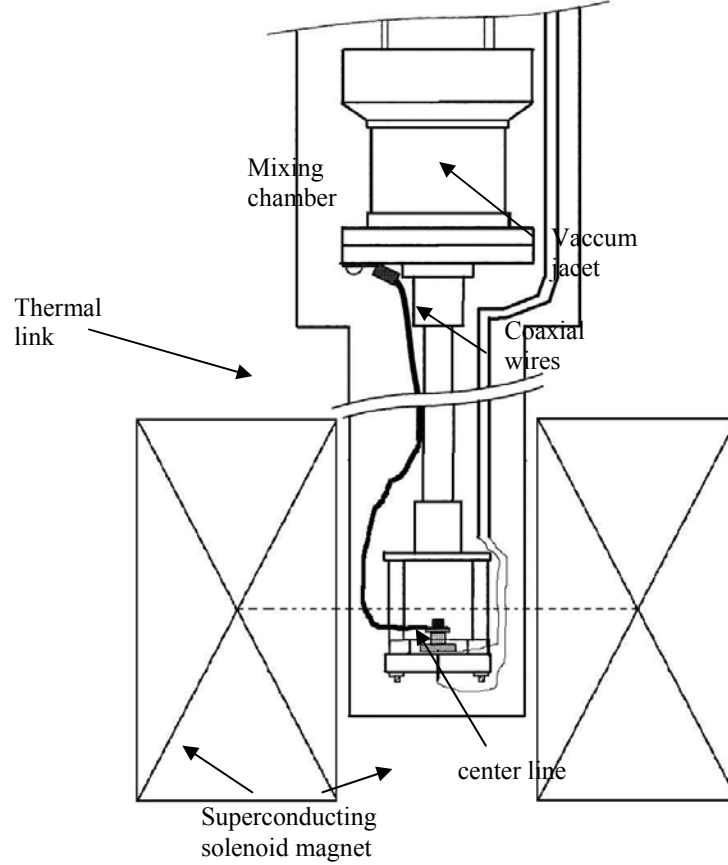


Figure 3.3.4: Schematic view of the load cell device, installed off-center of a solenoid magnet in a dilution refrigerator.

The natural field-gradient of the off-center position of a solenoid magnet was used (Fig. 3.3.4) [29]. It is reasonable to assume that the sample is so small, that \mathbf{M} does not vary spatially. If we neglect the radial term (because $M_r \ll M_z$, $B_r \ll B_z$, and because of the properties of the load cell - see Appendix C), from Eq. 3.3.1 the force on the load cell is:

$$\mathbf{F} = M_z \frac{dB_z}{dz} \hat{z} \quad (3.3.4)$$

The total capacitance response is then given by:

$$C_0^{-1} - C^{-1} = a \cdot M_z \frac{dB_z}{dz} \quad (3.3.5)$$

where a is a constant that depends on the elastic properties of the wires.

3.4 The Muon Spin Rotation (μ SR) Technique

A muon is an elementary particle which can have a negative or positive charge and has approximately 207 times the mass of an electron. It was first observed in cosmic rays by Carl D. Anderson and Seth Neddermeyer in 1936 [30], the year after the existence of a particle of about the same mass had been predicted by Hideki Yukawa. Since the muon is heavier, it differs from the electron in that it is unstable, decaying with an average lifetime of 2.2×10^{-6} sec into an electron or positron and a pair of neutrinos.

The μ SR technique allows one to study the magnetic properties of materials, through direct measurement of the time dependence of a positive muon (μ^+) polarization $P(t)$. In order to observe the relaxation of muon spins within a sample, it is clear that the incident muon beam should be polarized, and with sufficiently low energy to stop within a reasonable thickness of sample. The evolution of the polarization depends on the magnetic field that is experienced by the positive muon, and provides information on the magnetic environment in the vicinity of the muon. With this technique one can detect static magnetic fields as small as a fraction of a Gauss and as large as several Tesla and it is sensitive to magnetic fields fluctuating on a time scale of $10^{-3} - 10^{-11}$ sec.

3.4.1 Experimental Setup

The polarized muons are produced from pion decay (with pion lifetime $\tau_\pi = 26$ nsec) according to



Since only left-handed neutrinos exist, and because pions have zero spin, muons produced by pions at rest ($\vec{p}_p = 0$) have a spin \vec{s}_μ which is anti-parallel to their momentum \vec{p}_μ (See Fig. 3.4.1).

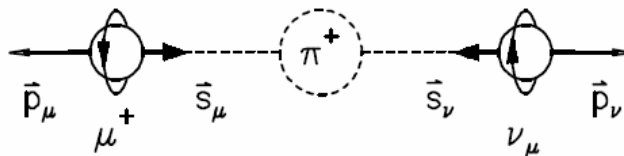


Figure 3.4.1: Schematic illustration of a positive pion decay into a muon and a neutrino (Taken from [31]).

These muons are guided into the sample by a set of dipole magnets, slow down and come to stop inside the sample within 10^{-10} sec. Then each muon decays into a positron and two neutrinos. Since most of the positrons are energetic enough to travel a substantial distance before annihilating, almost all of them reach the positron detectors.

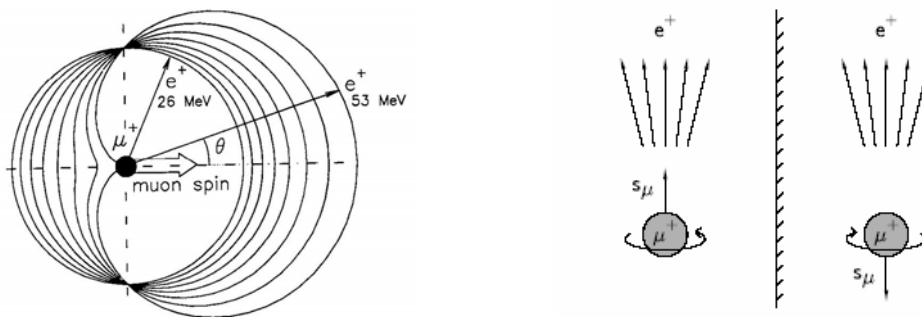


Figure 3.4.2: (a) Angular distribution of the positrons from the muon decay for various positron energies (Taken from [32]). (b) The mirror image of the muon decay. The direction of the muon-spin is reversed in the mirror so that the positrons are emitted predominantly in a direction opposite to that of the muon-spin. The violation of parity means that in our universe only the process on the left-hand side of the diagram is ever observed (taken from [33]).

The distribution of the decayed positrons is not spherically symmetric, but rather depends on the polarization of the muon; the positron is emitted preferably in the direction of the muon polarization as shown in Fig. 3.4.2a. This can be understood by considering the mirror image of the muon decay process (Fig 3.4.2b).

In this figure the length of the arrow represents the relative probability of positron emission in the direction of the arrow. The decay positrons are distributed about the muon spin direction according to the probability function:

$$W(\theta) = 1 + a \cdot \cos(\theta) \quad (3.4.2)$$

where θ is the angle between the muon spin and the direction of positron emission. The factor a increases monotonically with the positron energy, up to 52.83 MeV where $a = 1$. As one can see in Fig. 3.4.2a, positrons with low energy (~ 26 MeV) have no preference to the muon spin direction. However, very few positrons are emitted with such low energies and most of those that are will not be detected.

From the change in the angular distribution (as a function of time) of the emitted positrons, one can reconstruct the polarization of the muon as a function of time. When needed, a variable external magnetic field can also be applied: The longitudinal field configuration (LF) which is used to measure the rate in which the muon loses its polarization in the sample as a function of the magnetic field (H_L) applied along the direction of the initial muon polarization; and the transverse field configuration (TF) which is the one we used in our experiment.

3.4.2 The Transverse Field Configuration

The transverse field (TF) experimental configuration (Fig. 3.4.3) is used to measure both the frequency of the muon precession and the rate at which it loses its polarization as a function of the magnetic field (H_T), applied perpendicular to the muons initial spin direction. There are two ways to achieve this configuration:

1. The muon spin is applied parallel to the beam, and the field is applied perpendicular to it.
2. The muon spin is rotated by separators and the field is applied parallel to the beam. In this configuration the counters are placed to the left (L) and right (R) sides (or above and below) of the sample as shown in Fig. 3.4.3.

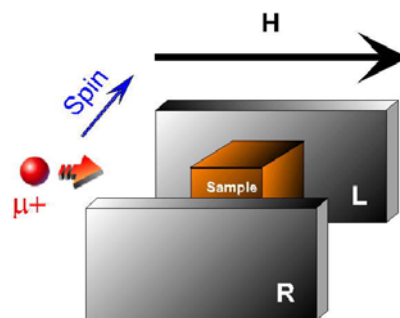


Figure 3.4.3: Transverse field setup.

3.4.3 Data Analysis

When the muons stop with a polarization along the beam direction \hat{z} , each muon spin evolves in the local field until the muon (μ^+) decays at a time t after its arrival. Two positron counters placed in the forward and backward directions with respect to \hat{z} are

used to obtain positron decay time histograms, which typically contain more than 10^6 events. The numbers of detected positrons in the backward and forward counters are correspondingly,

$$\begin{aligned} N_B(t) &= N_0^B \left[B_B + e^{-\frac{t}{\tau_\mu}} (1 + A_0 P_Z(t)) \right] \\ N_F(t) &= N_0^F \left[B_F + e^{-\frac{t}{\tau_\mu}} (1 - A_0 P_Z(t)) \right] \end{aligned} \quad (3.4.3)$$

where B_B (B_F) is the time independent background in the backward (forward) counter, N_0^B (N_0^F) is the counting rate in the backward (forward) counter, $P_Z(t)$ is the muon polarization in the \hat{z} direction as a function of time and A_0 is the asymmetry.

To extract the polarization function we subtract the constant background ($N_0^B B_B$ and $N_0^F B_F$), to obtain

$$\begin{aligned} B(t) &= N_B(t) - N_0^B B_B \\ F(t) &= N_F(t) - N_0^F B_F \end{aligned} \quad (3.4.4)$$

We define the experimental "raw" asymmetry as:

$$A_r(t) \equiv \frac{B(t) - F(t)}{B(t) + F(t)} = \frac{(1 - \alpha) + (1 + \alpha) A_0 P_z(t)}{(1 + \alpha) + (1 - \alpha) A_0 P_z(t)} \quad (3.4.5)$$

where α is the ratio of the raw count rates N_0^F / N_0^B , and reflects the ratio of the effective solid angles of the detectors. α can be calculated by applying a magnetic field which is transverse to the initial muon polarization, and finding the α value that gives oscillations centered around zero.

Finally, from equation (3.4.5) one can extract the corrected asymmetry which is proportional to the polarization in the \hat{z} direction

$$A(t) = A_0 P_z(t) = \frac{(1 - \alpha) + (1 + \alpha) A_r(t)}{(1 + \alpha) + (1 - \alpha) A_r(t)} = \frac{\alpha B(t) - F(t)}{\alpha B(t) + F(t)} \quad (3.4.6)$$

The polarization in the direction perpendicular to \hat{z} can be calculated from two positron counters placed to the left (L) and right (R) sides (or above and below) of the sample

$$A_\perp(t) = A_{\perp 0} P_\perp(t) = \frac{\alpha_\perp R(t) - L(t)}{\alpha_\perp R(t) + L(t)} \quad (3.4.7)$$

where $R(t)$ and $L(t)$ are the counts in the right (up) and left (down) counters after subtracting the background. α_{\perp} is the ratio between the raw count rate in the up detector to that in the down detector, N_0^R / N_0^L .

The asymmetry is fitted to the expected function from theoretical or phenomenological considerations, and the physical properties are extracted from the fitting parameters.

The arrangement of the positron counters and external field direction, longitudinal or transverse, is chosen depending on the information that we want to extract from the experiment.

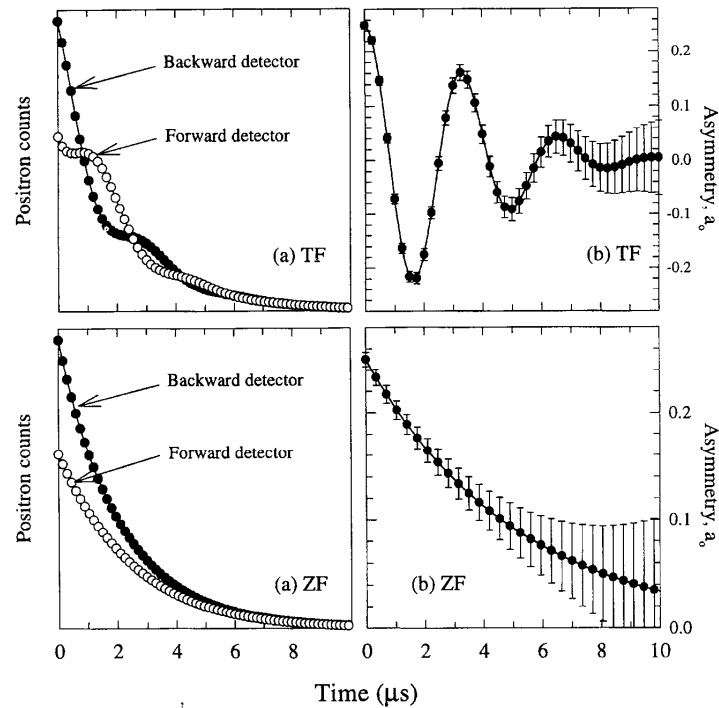


Figure 3.4.4: Simulated raw positron spectra in forward and backward detectors (a) for transverse field (TF) and longitudinal/zero field (ZF) geometries with the associated corrected asymmetry spectra (b). Taken from [32].

3.4.4 Muon Spin Rotation

The fully polarized muon, after entering the sample, comes to rest in a magnetic environment. Since the mechanism which stops the muon [33] is much stronger than any magnetic interaction, the muon maintains its polarization while losing its kinetic energy. However, at the stopping site the muon spin starts to evolve in the local field \mathbf{B} . When all

the muons experience a similar magnetic field at their sites, the polarization along the \hat{z} direction is given by

$$G_z(t) = \text{Re}\{\cos^2 \theta + \sin^2 \theta \cdot e^{i\omega(t-t_0)}\} \quad (3.4.8)$$

where θ is the angle between the initial muon spin and the local field direction (see Fig. 3.4.5), $\omega = \gamma_\mu |\mathbf{B}|$ is the Larmor frequency of the muon ($\gamma_\mu = 85.162$ MHz/kG), and t_0 is the stopping time of the muon.

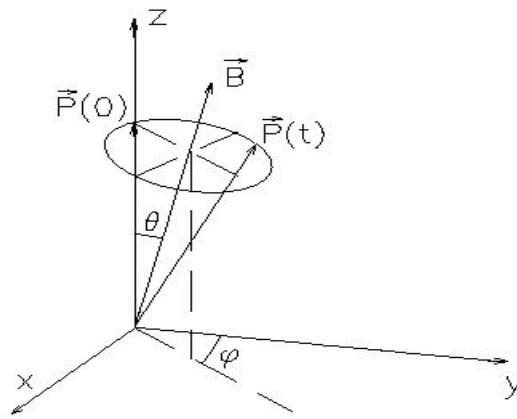


Figure 3.4.5: The muon polarization $\mathbf{P}(t)$ in the presence of a constant field \mathbf{B} .

In real systems, however, the local field experienced by different muons is rarely the same. It can vary from site to site as a result of nuclear moments, impurities, or non-homogeneous freezing of the ionic magnetic moments. It could also vary in time, at a given site, due to dynamic fluctuations. In these cases the oscillation amplitude decays. The decay or relaxation results from both dynamical fluctuations and spatial inhomogeneities.

Chapter 4

Experimental results

4.1 Faraday force magnetometer experiment

In this technique we measured two kinds of samples:

- One Fe₈ single crystal aligned so that its easy axis [9] is parallel to the applied magnetic field
- Several Fe₈ single crystals, glued on a small silver plate (with GE-varnish), and aligned so that their easy axis is parallel to the applied magnetic field (perpendicular to the silver plate).

4.1.1 One single crystal of Fe₈

The purpose of this experiment was to see the staircase shape of the magnetization in Fe₈, as a proof of its macroscopic quantum nature, and also as a precede try out to an experiment that will examine the influence of RF on the hysteresis loop.

The magnetization of the sample was measured in two configurations – first the sample was cooled down to $T \approx 40\text{mK}$ to examine the molecule in the pure quantum tunneling regime (which is $<400\text{mK}$) but with different sweeping rates of the magnetic field; Second, the sweeping rate was constant but the measurements were taken at different temperatures. In every measurement we first applied a high positive field ($H = 1.8\text{T}$) to magnetize the molecules in this direction, and then we swept the field to the negative regime.

On Fig. 4.1.1 the capacitance (in arbitrary units) vs. the magnetic field is presented at five different sweeping rates. The vertical dotted lines mark the matching fields, H_m , where the tunneling occurs. There are clearly three steps at sweeping rates 0.05 - 0.15 T/min that get smaller as sweeping rate is increased, until only the step at $\sim 0.22\text{T}$ is seen (One

should remember that $C \propto F \propto M \frac{\partial B_z}{\partial z}$, and because the sample is mounted off-center,

$\frac{\partial B_z}{\partial z}$ changes linearly with the field). We present one of these measurements in Fig 4.1.2

(the result of the measurement at 0.15T/min), where clear jumps are shown, marked by vertical lines.

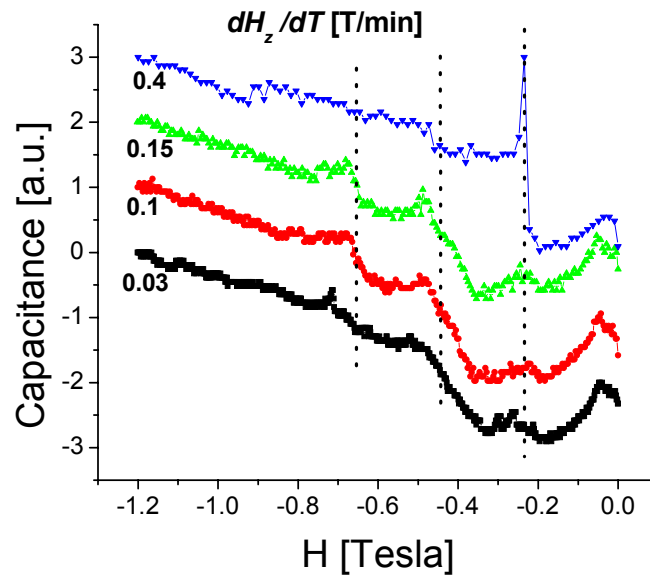


Figure 4.1.1: The capacitance (in arbitrary units) versus the magnetic field at five different sweeping rates (in ~ 40 mK, one single crystal). The vertical dotted lines are at the approximate matching fields $H_m \approx n \times 0.22$ T.

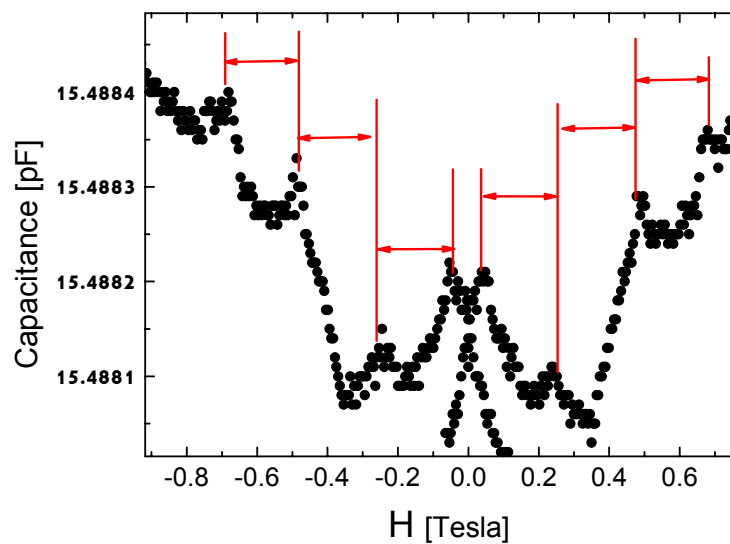


Figure 4.1.2: The capacitance versus the magnetic field ($dH/dt = 0.15$ T/min, $T = 40$ mK, one single crystal). One can see that the distance between steps is nearly constant (the arrows are of equal length).

Since the arrows in Fig. 4.1.2 are of equal length, one can see that the distance between steps is nearly constant. This fits the theoretical assumption about the equal separation between sequential matching fields (Eq. 2.4.1) and also previous experiments that have shown this phenomenon [1, 10, 11, 21].

In the second part of this experiment, we kept the sweeping rate constant (0.15 T/min) but raised the temperature. In Fig. 4.1.2 one can see that the measurements below 400mK are approximately the same as expected. When the temperature is increased above 400mK, the steps get smaller and less sharp until they vanish completely in 4.2K. These evidences show that the process that caused the jumps (= steps in the hysteresis loop) is quantum.

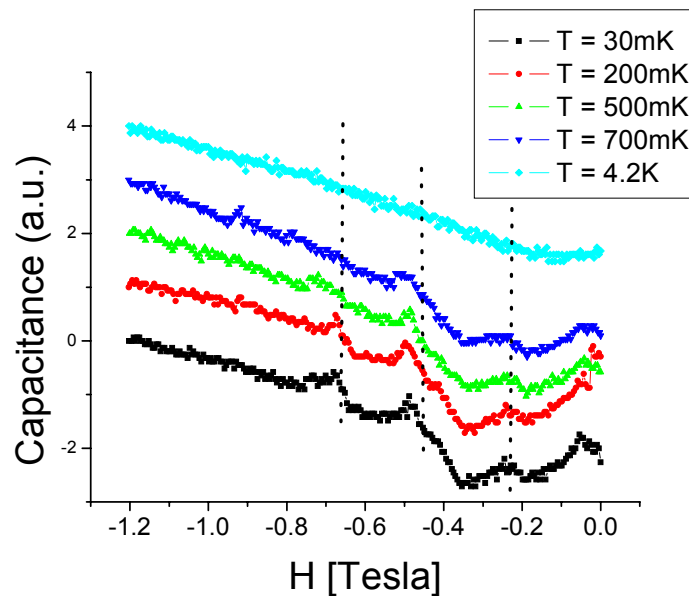


Figure 4.1.3: The capacitance (in arbitrary units) vs. the magnetic field at five different temperatures (constant sweep rate of 0.15T/min, one single crystal). The vertical dotted lines are at the approximate matching fields $H_m \approx n \times 0.22\text{T}$.

4.1.2 Mosaic of single crystals of Fe₈

We repeated the experiment with several Fe₈ single crystals, glued on a small silver plate, and aligned so that their easy axis is parallel to the applied magnetic field. The purpose of this experiment was to see whether several single crystals generate the same

result as one single crystal did (this sample was the one we used in the μ SR experiment, because the surface of one single crystal is too small for the muon beam, see sections 4.2.2-4.2.3).

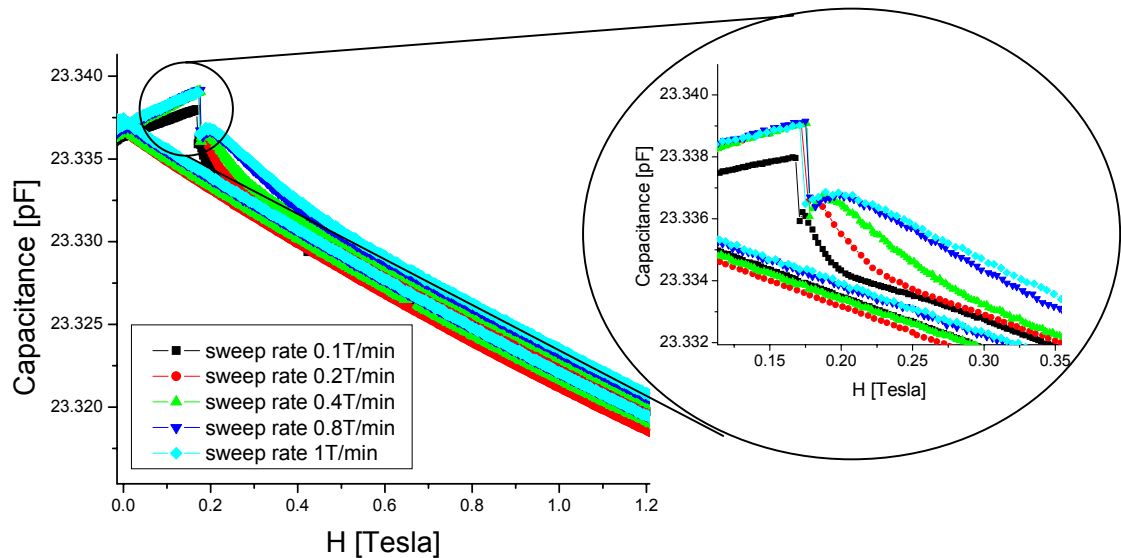


Figure 4.1.4: The capacitance versus the magnetic field in five different sweeping rates (in ~ 40 mK, mosaic of single crystals). One can notice that the higher the sweep rates, the smaller the jump.

In Fig 4.1.3 the capacitance vs. the magnetic field is shown for five different sweeping rates (in ~ 40 mK). In this experiment, as opposed to the one with one single crystal, there is only one step, which is in $H \approx -0.17$ T (and not near $H \approx -0.22$ T as expected).

4.1.3 Analysis of the faraday force magnetometer experiment

The capacitance was measured during the continuous sweep of the magnetic field, since stopping the sweep of the field is equivalent to measuring the QTM in zero sweeping rate. Whenever we stopped the field sweep, the capacitance changed abruptly, especially at high fields when we changed the direction of the sweep. This effect was probably caused by the time depending magnetic field which generated induced eddy currents in the copper disc of the movable plate. These currents changed the force acting on the load cell since the disc was also positioned (like the sample) in spatial varying magnetic field. Therefore, we could not analyze successfully the raw data by using the calibration of the load cell in order to calculate the magnetization of the sample. However, the jumps every

equally $\Delta H \approx 0.2T$ (Fig 4.1.2) that vanish at temperatures bigger than 1K (Fig. 4.1.3) prove qualitatively the quantum nature of the Fe8 single crystals.

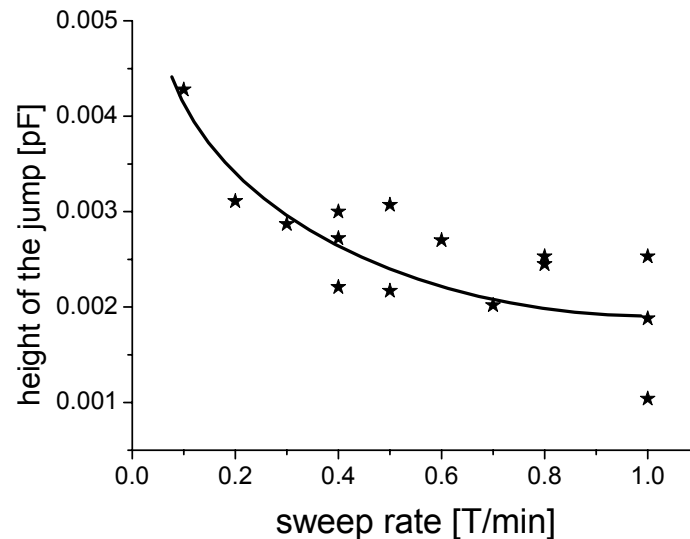


Figure 4.1.5: The height of the jump (in $H \approx 0.17T$) as a function of the sweeping rate. The solid line is a guide to the eye.

Another problem is that the sample was mounted off center. One may assume that the field is largest at the center of the magnet and gets weaker as you go out. However, in our magnets, with compensation turns, this might not be the case. Since this experiment is not done as it will be done in the future (with gradient coils that gives constant gradient during the sweep of the field with the sample in the center), we can only say that the fact that we see dependence on the sweep rate, even with the present crude set up, is encouraging for future development.

Although we couldn't determine the magnetization, we could analyze the data of the sample with several single crystals. When we measured the capacitance of this sample, we saw only one jump at $H \approx \pm 0.17T$. If we look on the height of the jump as a function of the sweeping rate (Fig. 4.1.4) we see that the jump gets smaller in higher sweeping rates. This fits the Landau-Zener model (which was represented in section 2.5), where the jump proportional to the tunneling probability. On the other hand, the jumps at the same

magnetic field in one single crystal (section 4.1.1) behave oppositely, but we have no explanation for that.

4.2 μ SR Experiment

The μ SR measurements were performed on a few Fe8 single crystals, glued on a small silver plate, and aligned so that their easy axis [9] was parallel to the direction of the muon beam (\hat{z} direction).

4.2.1 Experimental setup

We cooled down the crystals to a temperature of 40-100 mK to minimize activation effects (the tunneling process dominates below 400mK [1, 34]). The initial polarization of the muons was 50° relative to the \hat{z} axis, and the positron counters were rotated perpendicular to \hat{z} (Transverse Field setup) as depicted in Fig. 4.2.1. In this figure one can also see a possible direction of the magnetization and the internal magnetic field $\mathbf{B} = \mathbf{M} + \mathbf{H}$ around which the muon spin rotates. In this experimental configuration, the asymmetry is proportional to the muon spin polarization in the direction perpendicular to the \hat{z} axis.

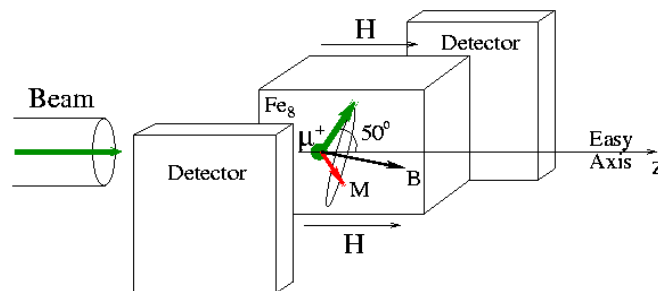


Figure 4.2.1: The arrangement of the Fe8 single crystal in the experimental apparatus.

At the matching fields in Fe8, tunneling can take place between spin states of opposite polarization. When the magnetic field \mathbf{H} is very different from the matching field $H_m(n)$, these transitions are suppressed. This property can be utilized to prepare the system in a number of different spin configurations, which are stable for a long time (see below), by

cycling an external magnetic field, even though at the end of the cycle the field is always the same.

For the preparation of various spin states we utilize a three step field cycle [35, 36]. It starts by applying a strong negative field of -1.5T parallel to \hat{z} for 10 minutes to polarize the Fe8 molecules. In such a strong field all the spins are in their $S_z = -10$ state. The field is then swept to an intermediate positive value H_i , at a rate of 0.245 T/min , crossing a matching field during the process, and, as a consequence, populating states with positive S_z . Finally, the field is swept back to $+0.005\text{T}$, crossing some matching fields again (The field is swept to a value close to and not exactly zero since $H = 0\text{T}$ is one of the matching fields). The important aspect of the μSR experiment is that the measurement is done always at the same field and only H_i varies.

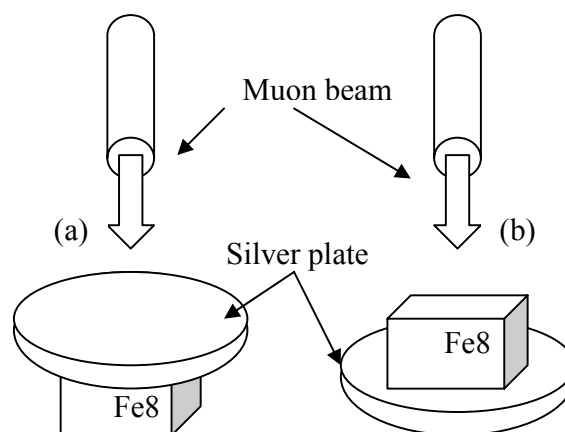


Figure 4.2.2: (a) In the first experiment the muons stopped in the silver plate; (b) in the second experiment some of them stopped in the sample or the GE-varnish between the crystals.

The Fe8 single crystals, glued on a small silver plate, were positioned in two different structures:

- The sample was positioned beneath the silver plate (meaning the muons hit the silver plate, Fig 4.2.2a)
- The sample was positioned above the silver plate (meaning the muons hit the sample, Fig 4.2.2b).

4.2.2 Muons hit the silver plate - Results

In this experiment, the muons hit the silver plate (0.5mm) and not the sample itself. As a result, the asymmetry was high (all the muons could be detected, see appendix D), but on the other hand, the muons were stopped 0.375mm from the sample (the muon can penetrate only up to 0.125mm from the surface of the silver). Therefore, the magnetic fields that the muons sense due to the magnetization of the sample is respectively low.

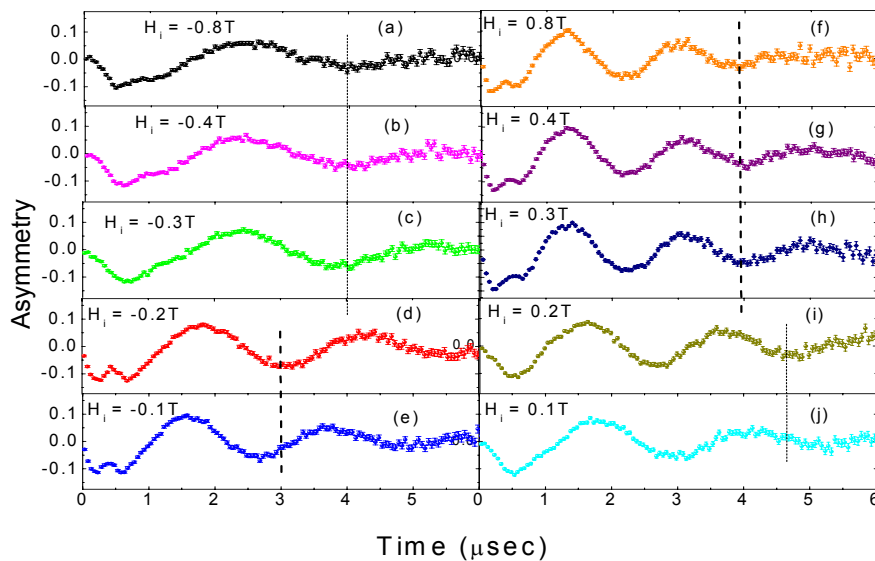


Figure 4.2.3: Measurement on Fe8 using μ SR (muons hit the silver). Different intermediate fields (H_i) lead to different muon rotation frequencies. The difference is most noted comparing $H_i=0.2T$ (-0.2T) to $H_i=0.3T$ (-0.3T).

In Fig. 4.2.3, panels (a) to (j), the asymmetry is shown as a function of time for ten different intermediate fields H_i (the asymmetry is proportional to the muon spin, see section 3.4.3). The results of the experiments with negative fields H_i are on the left side (a-e) of the graph, while on the right side (f-j) we present the results with positive fields. There is a major difference in the muon asymmetry between panels (c) to (d) and panels (h) to (i), meaning between $H_i=0.2T$ (-0.2T) to $H_i=0.3T$ (-0.3T). Here we see that different intermediate fields cause significantly different precession frequencies of the muon spin. This is emphasized by the vertical dotted line passing through the second minimum of the negative H_i run and the third minimum of the positive H_i runs. Also in

panels (d) to (h) two oscillations are observed that correspond to two frequencies - one high (up to 11 MRad/sec) and one low [no more than 3.7 MRad/sec] ; the high frequency has fast relaxation and it disappears very quickly.

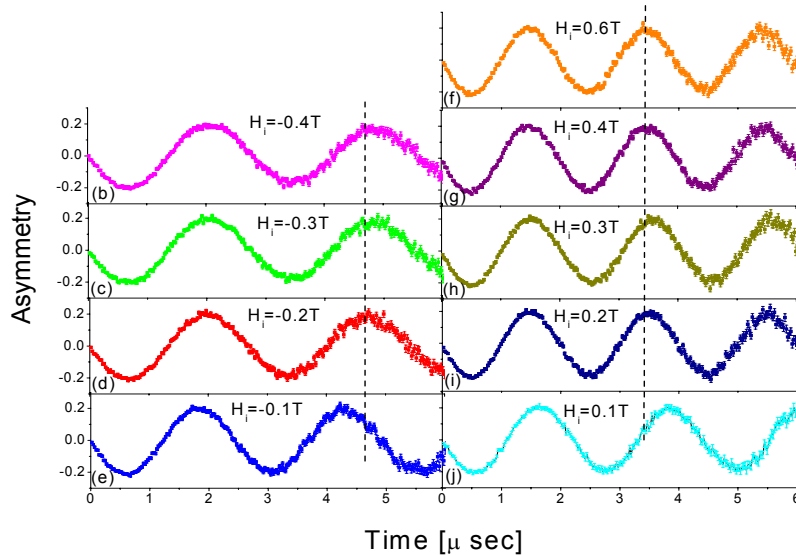


Figure 4.2.4: Measurement in an empty holder. Due to flux trapping in the magnet, different intermediate fields (H_i) lead to different muon rotation frequencies in low magnetic fields, but to similar frequencies in high fields (muons hit the silver plate).

Since the experiment was performed with a superconducting magnet, we did a test experiment with an empty sample holder (without Fe8 crystals). The test experiment was performed because a superconducting magnet, like the one we use, could have trapped flux, leading to a slightly different measurement of the field for different intermediate fields, even though we always program the magnet power supply to produce 50 G ($=0.005T$) at the end of the field cycle. The results of these test experiments are summarized in Fig. 4.2.4, panels (b) to (j). It presents the asymmetry as a function of time for a test case of the sample holder without the sample, in some different intermediate fields H_i . The results of the experiments with negative H_i are on the left side (b)-(e) of the graph, while on the right side (f)-(j) the experiments with positive H_i are presented.

4.2.3 Muons hit the silver plate - Analysis

We analyzed the data by fitting the asymmetry of all runs both with and without the sample to a function of the form:

$$A(t) = A_h \sin(\omega_h t) e^{-\lambda_h t} + A_l \sin(\omega_l t) e^{-\lambda_l t} \quad (4.2.1)$$

The precession frequencies indicate the magnetic field, $\mathbf{B} = \gamma_\mu \boldsymbol{\omega}$, experienced by the muon, where $\gamma_\mu = 2\pi \cdot 13.554$ kHz/G is the muon gyromagnetic ratio. The subscript h (l) stands for high (low) frequency and high (low) relaxation. Some of the high frequencies as a function of the intermediate fields are shown in the inset of Fig. 4.2.5. As one can see, despite the noisy data there is some indication of steps which is emphasized by the horizontal lines.

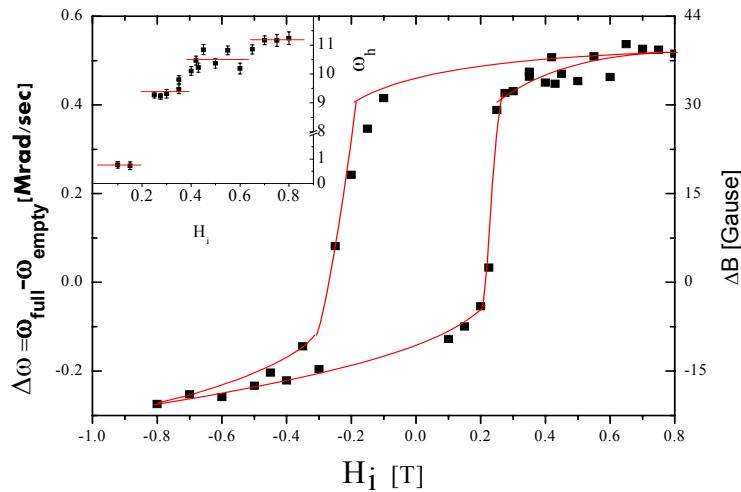


Figure 4.2.5: The shift change in the muon rotation frequency as a function of the intermediate field H_i , between an empty sample holder, and a holder with Fe8. Raw data of ω_h versus H_i is shown in the inset. The solid lines are a guide to the eye.

In Fig. 4.2.5 we present the frequency shift $\Delta\omega$ between the measurements on the empty holder and on Fe8 (the low frequencies). The shift is the largest at high intermediate fields, and it changes drastically in the regime of $H_i = \pm 0.2$ T. Despite the fact that the measurements were always done under the same conditions (magnetic field of 0.005 T) a hysteresis loop could be observed.

4.2.4 Muons hit the sample - Results

In this case the muons are in the sample, the varnish, or the silver plate. In Fig. 4.2.6, panels (a) to (f), we present the asymmetry as a function of time for two setups, and three different intermediate fields H_i . The results of the experiments with Fe8 crystals are on the left side (a-c) of the graph, while on the right side (d-f) we present a test case of the sample holder without the sample. As mentioned in section 4.1.2, we performed test experiments because a superconducting magnet could have trapped flux.

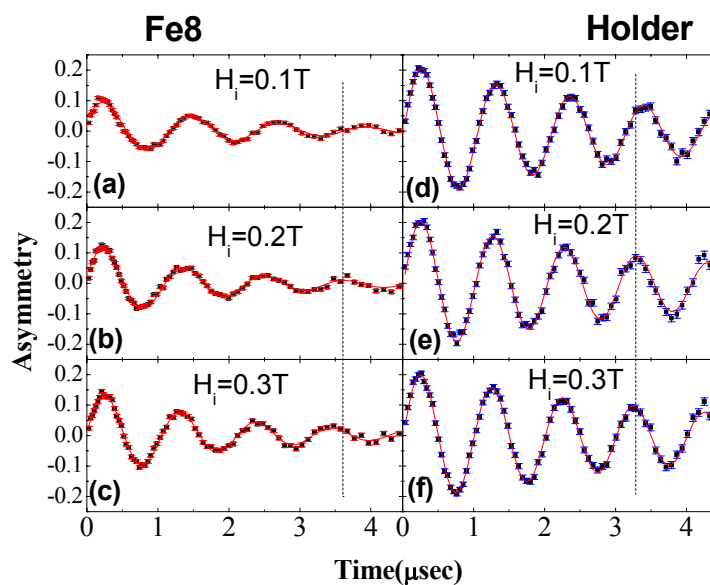


Figure 4.2.6: Different intermediate fields (H_i) lead to different muon rotation frequencies in Fe8 (a, b & c), but to similar frequencies in an empty holder (d, e & f).

The most noticeable variation in Fig. 4.2.6 is the difference in amplitude between the experiment with the Fe8 sample and the one with an empty holder (explanation in Appendix D). A more important but subtle change in the data is the difference in the muon asymmetry between runs with the sample, panels (a) to (c). Here we see that different intermediate fields cause different precession frequencies of the muon spin. This is emphasized by the vertical dotted line passing through the fourth maximum of the $H_i = 0.2$ T run [panel b]. For comparison, the fourth maximum of the $H_i = 0.1$ and 0.3 T [panels (a) and (c)] are a quarter of wavelength to the left and to the right of this line, respectively. In contrast, the situation in the test case, panels (d) to (f), is different. There

is no noticeable difference in the muon asymmetry between the intermediate fields $H_i = 0.2$ and 0.3 T [panels (e) to (f)], and only a small difference between the $H_i = 0.1$ and 0.2 T cases. This suggests that most of the frequency shift is due to the Fe8 molecules.

4.2.5 Muons hit the sample - Analysis

We analyzed the data by fitting the asymmetry of all runs both with and without the sample to a function

$$A(t) = A \sin(\omega t) e^{-\lambda t} \quad (4.2.2)$$

where $\mathbf{B} = \gamma_\mu \boldsymbol{\omega}$. In this experiment, as opposed to the one where the muons hit the silver plate, there was only one frequency.

The frequencies for both the sample and the holder as a function of the intermediate fields are shown in the inset of Fig. 4.2.7.

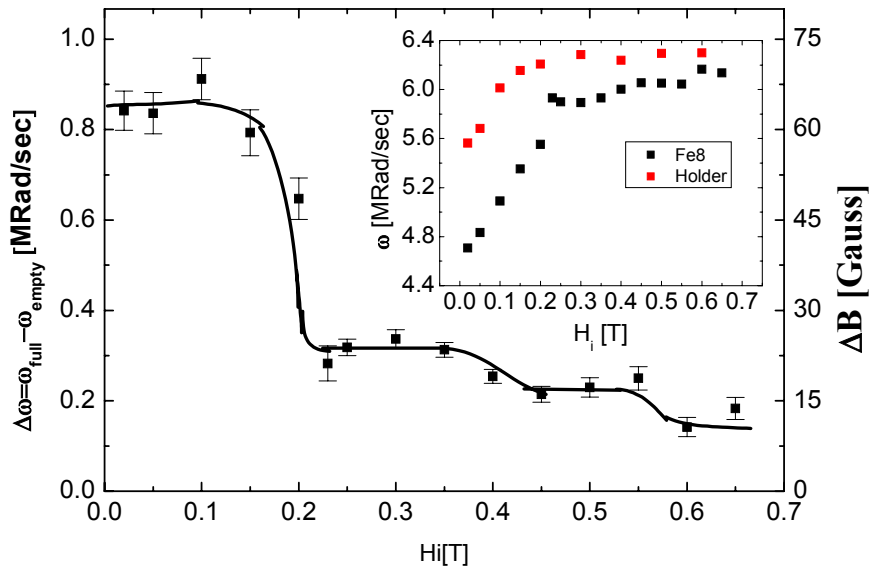


Figure 4.2.7: The change in the muon rotation frequency between an empty sample holder, and a holder with Fe8 as a function of the intermediate field H_i ($\Delta\omega$ is proportional to the magnetic field generated by the sample). Raw data of ω versus H_i with, and without, Fe8 is shown in the inset (muons hit the sample). The solid line is a guide to the eye.

In this inset one can see that the frequency changes between the measurements with and without the sample. It seems that when intermediate fields smaller than 0.1 T are used, the trapped flux in the magnet is more significant (the frequency decreases abruptly in this region).

Fig. 4.2.7 is the major figure of the thesis, where the frequency shift $\Delta\omega$ between the empty holder and our measurements on Fe8 is presented. If we translate the frequency into magnetic field, we get:

$$\Delta B = B_{Fe_8} - B_{Holder} = \frac{\omega_{Fe_8}(H_i) - \omega_{Holder}(H_i)}{\gamma_\mu} \quad (4.2.3)$$

where ΔB is the shift in the magnetic field which is the field created by the sample (the right axis in Fig. 4.2.7). The solid line is a guide to the eye. The shift is the largest at low H_i and decreases sharply when H_i increases toward the first matching field of ~ 0.22 T. Upon further increase of H_i , ΔB stays flat until a second decrease occurs slightly above 0.4T. This situation repeats itself above 0.6T.

It is important to mention that the same measurements have been repeated more than once in order to prove that the results are reproducible. Performing the same field cycle twice always gave exactly the same muon behavior both with and without the sample. This reassured us that, although the field produced by the superconducting magnet depended on H_i , the shift was reproducible.

Chapter 5

Discussion and summary

5.1 Comparison to the Landau-Zener model and to previous experiments

According to the Landau-Zener model (section 2.5) the tunneling probability P when sweeping the longitudinal field H_z at a constant rate over an avoided energy level crossing

(inset in 2.4.1) is given by $P = 1 - \exp\left[-\frac{\pi\Delta_{m,m'}^2}{2\hbar g\mu_B|m-m'|dH/dt}\right]$ (Eq. 2.5.1), where $\Delta_{m,m'}$ is

the tunnel splitting, m and m' are the quantum numbers of the avoided level crossing, and dH_z/dt is the constant field sweeping rates.

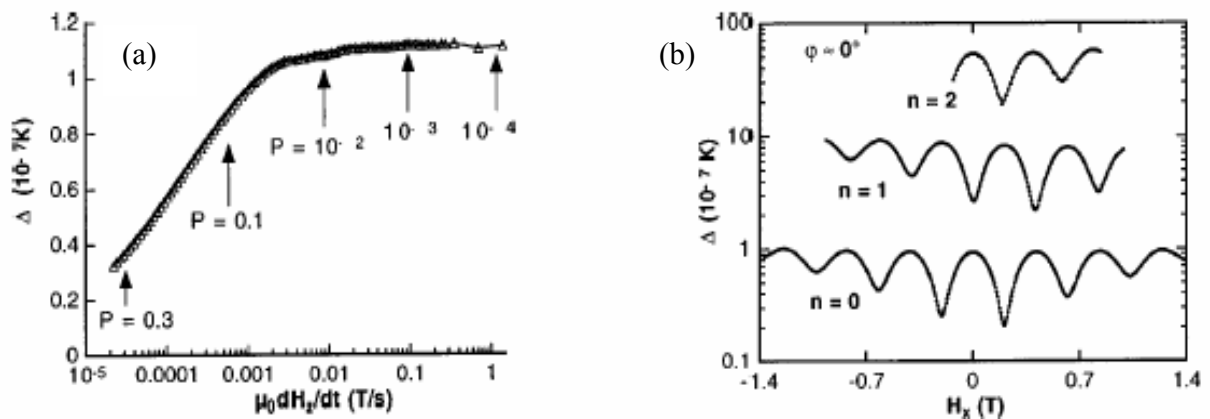


Figure 5.1.1: (a) Field sweeping rate dependence of the effective tunnel splitting Δ measured by the Landau Zener method. The measured Landau-Zener tunneling probability P is indicated for several field sweeping rates. (b) Measured tunnel splitting Δ as a function of transverse field for $\varphi=0^\circ$ (H_z is parallel to the easy axis), and for the quantum transition between $M = -10$ and $(S - n)$. From [11, 21].

Wernsdorfer et al [11] have measured the tunnel splitting $\Delta_{-10,10}$ for many different sweeping rates (Fig 5.1.1a). The Landau-Zener model predicts that all the measurements of this tunnel splitting should give constant result, which was indeed the case for sweeping rates between 1 and 0.001T/s. Wernsdorfer also measured $\Delta_{-10,10-n}$ for

$n = 0,1,2$ (Fig 5.1.1b) as a function of the transverse field applied parallel to the hard axis. It shows that the tunnel frequency has a minima when the transverse field is varied, which is in agreement with theoretical predictions [15] that the tunnel splitting vanishes for certain values of H_x (where \hat{x} is the direction of the hard axis). However, these theoretical predictions do not take into account the fact that a spin is also subject to hyperfine interactions, dipole-dipole interactions and spin phonon interactions. As a result, in practice, the minima of $\Delta_{m,m'}$ does not vanish as seen in Fig 5.1.1b.

If we substitute the tunnel splitting ($\Delta_{m,m'}$) from Wernsdorfer experiment (Fig. 5.1.1b) into the Landau-Zener model (Eq. 2.5.1), and substitute also: $\hbar = 7.6328 \times 10^{-12} [K] \cdot [s]$, $\mu_B = 0.67170099 [K]/[T]$, and $dH/dt = 0.245 [T]/[\text{min}] = 4.083 \times 10^{-3} [T]/[s]$ which

gives $\frac{\pi}{2g\hbar\mu_B dH/dt} = 3.752 \times 10^{13} [K^{-2}]$, we get that:

- For $\Delta_{-10,10} = 10^{-7} \text{ K} \rightarrow P_{-10,10} \approx 0.02$,
- For $\Delta_{-10,9} = 3 \times 10^{-7} \text{ K} \rightarrow P_{-10,9} \approx 0.16$,
- For $\Delta_{-10,8} = 20 \times 10^{-7} \text{ K} \rightarrow P_{-10,8} \approx 0.9998$.

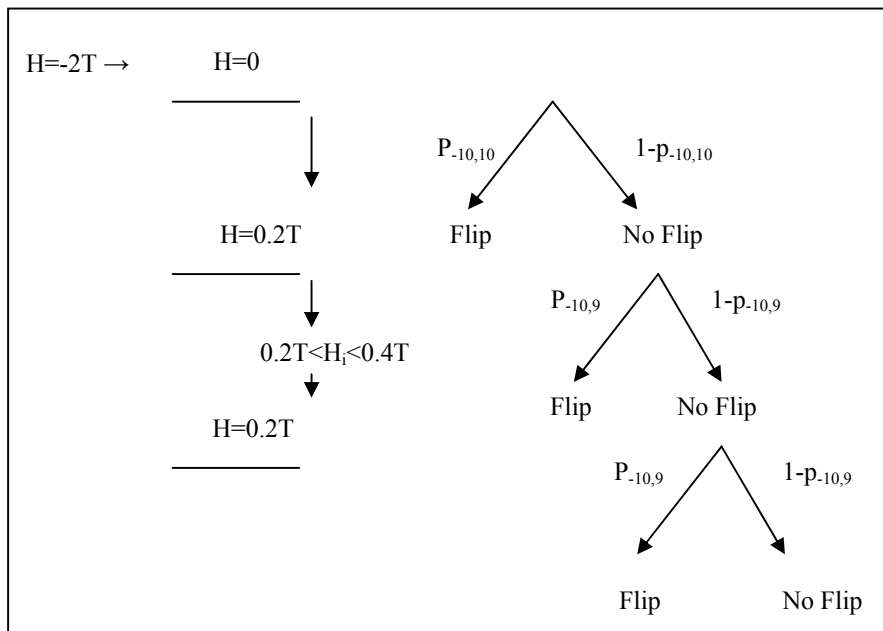


Figure 5.1.2: Schematic diagram of the probability to tunnel from $m = -10$ to $m' = 10, 9$, during a three field cycle experiment with $0.2T < H_1 < 0.4T$. The probability not to tunnel is given by: $(1 - P_{-10,10}) \times (1 - P_{-10,9})^2$.

In our μ SR experiment we applied a strong magnetic field at the beginning of every measurement, so 100% of the molecules were in the $S_z = -10$ state (up). Then we swept the field to an intermediate value, and finely to 0.005T. The shift $\Delta\omega$ (Fig 4.2.7) is proportional to the difference in the probability between up and down states. We concentrate on the shift jump for intermediate field below 0.22T and above it, see Fig. 5.1.2. In this figure $H=0$ T stand for the $-10,10$ transition, and $H=0.22$ T represent the $-10,9$ transition. The populations after the cycle are:

$$\begin{aligned} P_{up} &= p_0 + (1-p_0)p_1 + (1-p_0)(1-p_1)p_1 \\ P_{down} &= (1-p_0)(1-p_1)(1-p_1) \end{aligned} \quad (5.1.1)$$

One can see that the sum of the two probabilities is 1 and in the specific case the probabilities are $P_{down}=0.69$ and $P_{up}=0.31$.

In order to connect between the shift and these populations we need to introduce a base line correction constant, ω_{corr} , since the hysteresis loop is not symmetric around zero (see Fig 4.2.7). We therefore write:

$$\Delta\omega(H_i) - \omega_{corr} = C(P_{up}(H_i) - P_{down}(H_i)) \quad (5.1.2)$$

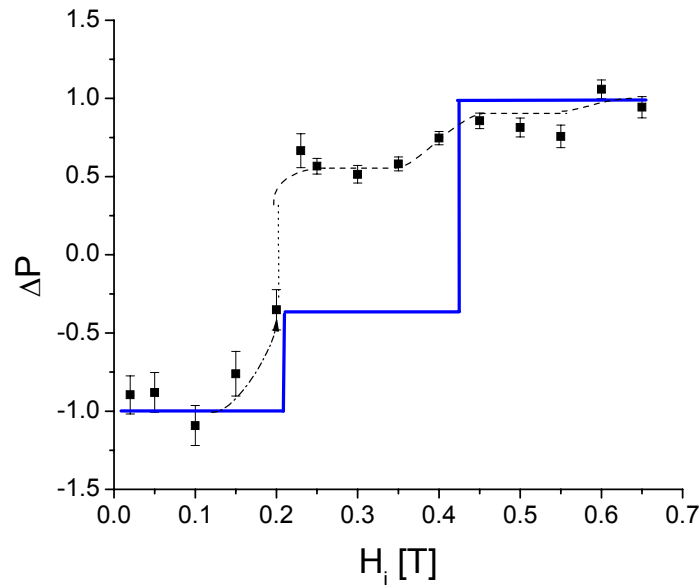


Figure 5.1.3: Our μ SR results on Fe8, $(2\Delta\omega(H_i) - \Delta\omega_0 - \Delta\omega_\infty)/(\Delta\omega_\infty - \Delta\omega_0)$, with the dotted line as a guide to the eye, and theoretical prediction (solid blue line) due to the Landau Zener model, $P_{up}(H_i) - P_{down}(H_i)$. The steps appear at the right place but not with the predicted height.

We have two known limits: at $H_i = 0$, $P_{down} = 1$ so $\Delta\omega_0 = C + \omega_{corr}$; at high H_i , $P_{down} = 0$ so $\Delta\omega_\infty = \omega_{corr} - C$. This gives:

$$\frac{\Delta\omega_0 + \Delta\omega_\infty}{2} = \omega_{corr} \quad \frac{\Delta\omega_0 - \Delta\omega_\infty}{2} = C \quad (5.1.3)$$

Finally we get:

$$\frac{2\Delta\omega(H_i) - \Delta\omega_0 - \Delta\omega_\infty}{\Delta\omega_\infty - \Delta\omega_0} = P_{up}(H_i) - P_{down}(H_i) = \Delta P \quad (5.1.4)$$

In Fig. 5.1.3 we plot ΔP . The solid line represents the expected behavior if shift changes would occur only at matching field according to the LZ theory described above. This line does not agree very well with our experiment. However, it is clear that shift changes occur even without crossing matching fields due to relaxation processes, especially between 0 and 0.22T. If we compare ΔP only with the actual jump, we find a better agreement as shown by the dotted line.

Another possible cause for the discrepancy is the orientation of the crystals. The easy axis of Fe8 is 16° from the \hat{a} axis (Fig 1.2.1), and it is very hard to align many of them (~ 20) correctly. In that case, there is a component of the applied field parallel to the hard axis.

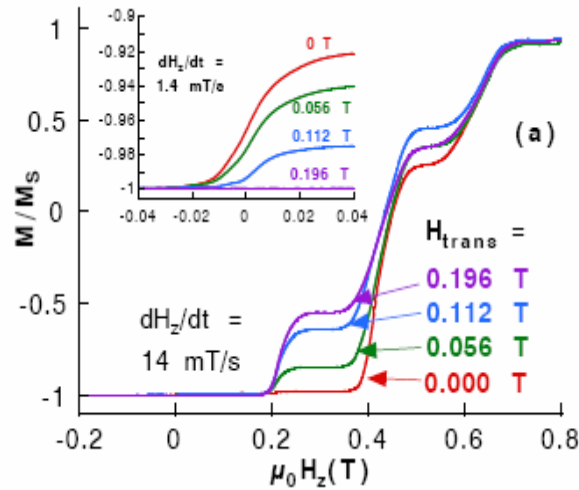


Figure 5.1.4: Hysteresis loops measured by Wernsdorfer [11] in the presence of a constant transverse field, at 0.04 K. Insets: Enlargement around the field $H=0$. Notice that the sweeping rate is ten times slower for the measurements in the insets than that of the main figures.

Moreover, crystals that are not aligned with their easy axis parallel to \hat{z} , have some component of the magnetization in the perpendicular direction, which creates magnetic fields in that direction, and influence the neighboring crystals. These perpendicular components cause an increase in $\Delta_{-10,9}$ and decrease in $\Delta_{-10,8}$ (as shown in Fig 5.1.1b) which means increase in $P_{-10,9}$ and decrease in $P_{-10,8}$. The increase in $P_{-10,9}$ can explain the bigger jump at $\sim 0.22\text{T}$ and therefore the smaller jump at $\sim 0.44\text{T}$. Another way to show the effect of the transverse field on the hysteresis loop is presented in Fig 5.1.2 (also from Wernsdorfer et al [11]). One can see a significant increase of the step at $\sim 0.22\text{T}$ with the presence of a transverse field and a significant decrease of the step at $\sim 0.44\text{T}$.

Nevertheless, even if we take into account the fact that we pass every intermediate field twice, and $P_{-10,9}$ is twice the theoretical value, we still can't explain the small jump in $H \approx 0.4\text{T}$ (as compared to the $H \approx 0.22\text{T}$ jump). However, it is important to note that also in the Faraday force magnetometer experiment with the same mosaic sample, only the 2kG was detected.

5.2 The difference between Fe8 and a regular magnet

The same process and measurement (first saturation at $H = -1.5\text{T}$, then sweeping the field to a positive intermediate field H_i and finally measuring the magnetization at zero field) was done on SmCo, a regular permanent magnet with a similar saturation field (fig. 5.2.1a). As expected, there is only one plateau in the beginning (when H_i is smaller than the cohesive field) and then a monotonic and almost linear decrease. This is why a regular magnet can function as a binary unit – it has only two stable clear states (only one plateau in each direction of the process, saturating in negative or positive field).

As opposed to SmCo, in Fe8 we showed [Fig 5.2.1b] that there are at least six stable states (considering both sides of the hysteresis loop), which is twice more than in SmCo. Hence Fe₈ can “remember” which intermediate field was visited, and this memory lasts at least on the time scale of the μSR measurement (approximately 1/2 hour). In fact, we have preliminary data showing that this memory lasts at least for several hours (not shown).

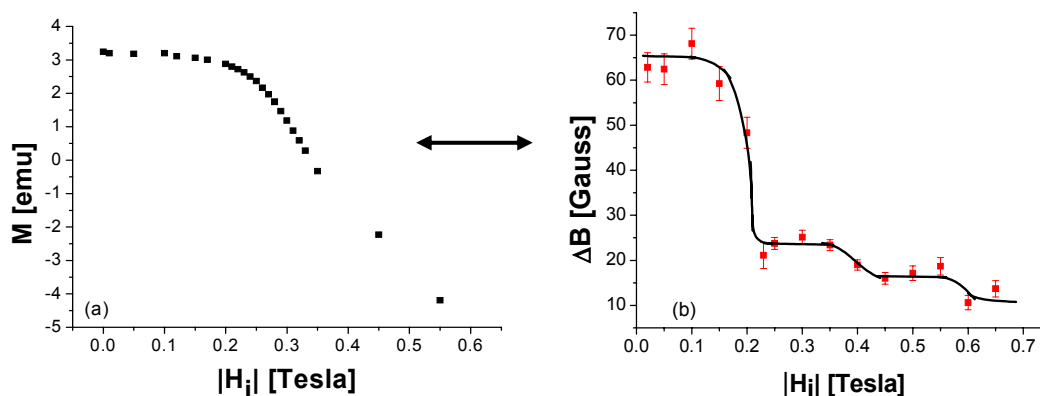


Figure 5.2.1: The same experiment ($1.5T \rightarrow H_i \rightarrow$ measurement in 50G) has been done on SmCo (a), a regular permanent magnet with similar saturation field. There is only one plateau compare to Fe8 with 2-3 plateaus (b).

5.3 Summary

In this thesis the quantum nature of Fe8 high spin molecules was studied using the Faraday force magnetometer and the μ SR technique. All the measurements were performed in a dilution refrigerator (DR) to achieve sub-kelvin temperatures, some of them in a first time operated DR.

The qualitative result from the Faraday force magnetometer demonstrated again the known behavior of the Fe8 single crystals. The measurement of the capacitance as a function of the magnetic field showed clear steps which reveal the quantum behavior of the molecules in a macroscopic examination. We have seen that the steps occurred in “matching” fields ($H_m \approx n \times 0.22T$) and they depended on the sweep rate, as the Landau-Zener model predicts. Above ~ 400 mK, the steps also depended on the temperature, giving rise to thermally assisted tunneling. The results from a mosaic sample of several Fe8 single crystals showed only one step (at $H \approx 0.2T$), as opposed to the results from one single crystal, apparently because the lack of orientation of the crystals. This measurement was important because we used this sample for the μ SR experiment.

Using the μ SR technique, which is also applicable to films, we observed quantum tunneling of the magnetization (QTM) in the Fe8 compound. We swept the external

magnetic field applied on the Fe₈ sample from -1.5 T, to some intermediate field (H_i), and then to 50 G (=0.005T) at $T = 40$ mK where no thermal activation occurs. The precession frequency of muons in the sample changed depending on the value of H_i . QTM was observed in the form of steps in the frequency as a function of H_i , which reflects tunneling between different spin states of the Fe₈ molecules in the vicinity of the muon. These steps coincide with the matching fields, at which different molecular spin states of different directions, up or down, have the same energy and therefore the molecular spin can tunnel between them. It is this recollection of H_i , and the fact that many final frequencies can be prepared, which warrants Fe₈ molecules the candidacy for a multi-bit magnetic memory.

Appendix A

Non Adiabatic Transition explained by Landau and Zener [10, 11, 18, 19]

Let's consider the crossing of energy levels of the two electron eigenstates ψ_1 and ψ_2 for an unperturbed Hamiltonian \mathcal{H}_0 as can be schematically shown in Fig.A.1.

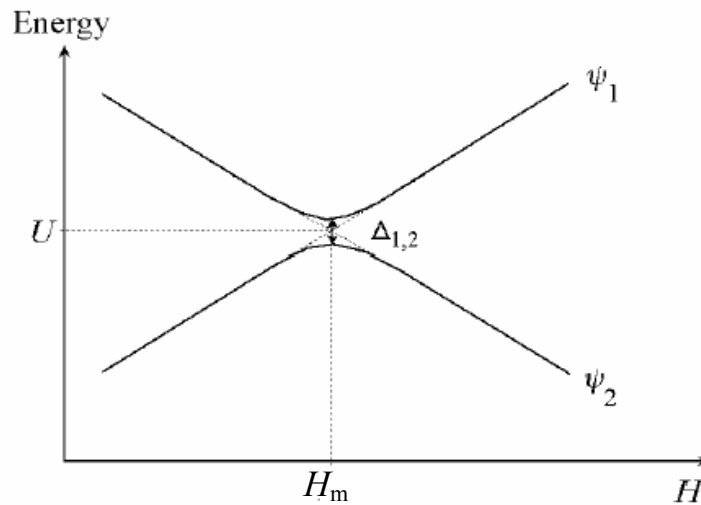


Figure A.1: Crossing of energy levels.

The schrödinger equations for ψ_1 and ψ_2 can be written as,

$$\begin{aligned}\mathcal{H}_0\psi_1 &= U_1\psi_1 \\ \mathcal{H}_0\psi_2 &= U_2\psi_2\end{aligned}\tag{A.1}$$

where U_1 and U_2 are eigenvalues for ψ_1 and ψ_2 , respectively. An eigenfunction for schrödinger equation is assumed to have a form

$$i\hbar\frac{d\psi}{dt} = (\mathcal{H}_0 + \mathbf{V})\psi\tag{A.2}$$

where \mathbf{V} is a perturbation term, and

$$\psi = b_1\psi_1 + b_2\psi_2\tag{A.3}$$

Substituting eq.(A.3) into eq. (A.2), we get

$$\begin{aligned} i\hbar \frac{db_1}{dt} &= (U_1 + V_{11})b_1 + V_{12}b_2 \\ i\hbar \frac{db_2}{dt} &= (U_2 + V_{22})b_2 + V_{12}b_1 \end{aligned} \quad (\text{A.4})$$

where V_{ik} is $\int \psi_i^* \mathbf{V} \psi_k dr$. Near the energy level crossing point, $U_1 + V_{11}$ and $U_2 + V_{22}$ can be expressed by a parameter $\xi = H(t) - H_m$ as,

$$\begin{aligned} U_1 + V_{11} &= U - F_1 \cdot \xi \\ U_2 + V_{22} &= U - F_2 \cdot \xi \end{aligned} \quad (\text{A.5})$$

where U is a common value of $U_1 + V_{11}$ and $U_2 + V_{22}$ at the energy level cross point, $F_1 = -\partial(U_1 + V_{11})/\partial\xi$ and $F_2 = -\partial(U_2 + V_{22})/\partial\xi$. By using new parameters a_1 and a_2 , we can write b_1 and b_2 as:

$$\begin{aligned} b_1 &= a_1 \exp\left(-\frac{i}{\hbar} U \cdot t\right) \\ b_2 &= a_2 \exp\left(-\frac{i}{\hbar} U \cdot t\right) \end{aligned} \quad (\text{A.6})$$

Further changing the differentiation with t by the differentiation with ξ as $\frac{d}{dt} = \frac{d\xi}{dt} \cdot \frac{d}{d\xi}$,

the equations (A.4) can be rewritten as

$$\begin{aligned} i\hbar v \frac{da_1}{d\xi} &= -F_1 \xi a_1 + V_{12} a_2 \\ i\hbar v \frac{da_2}{d\xi} &= -F_2 \xi a_2 + V_{12} a_1 \end{aligned} \quad (\text{A.7})$$

where $v = d\xi/dt = dH/dt$.

The solution of eq.(A.7) at $t = -\infty$, $|a_1(-\infty)|^2$ under initial conditions $a_1(-\infty) = 1$ and $a_2(-\infty) = 0$ means a probability of a state remains in the ψ_1 state through the level crossing point of $\xi=0$. The solution $|a_1(-\infty)|^2$ is given as [18]

$$|a_1(-\infty)|^2 = \exp\left(-\frac{2\pi V_{12}^2}{\hbar v |F_2 - F_1|}\right) \quad (\text{A.8})$$

For the case of QTM under the magnetic field H , the Hamiltonian \mathcal{H}_0 can be written as

$$\mathcal{H}_0 = DS_z^2 + g\mu_B H_z S_z \quad (\text{A.9})$$

and the eigenvalues for the eigenstate ψ_1 and ψ_2 are:

$$\begin{aligned} U_1 &= g\mu_B H m_1 \\ U_2 &= g\mu_B H m_2 \end{aligned} \quad (\text{A.10})$$

Then, assuming V_{11} and V_{22} are independent of H , F_1 and F_2 are given as,

$$\begin{aligned} F_1 &= -\frac{\partial(U_1 + V_{11})}{\partial\xi} = -g\mu_B m_1 \\ F_2 &= -\frac{\partial(U_2 + V_{22})}{\partial\xi} = -g\mu_B m_2 \end{aligned} \quad (\text{A.11})$$

On the other hand, the energy gap $\Delta_{1,2}$ at the energy level crossing point is given as

$$\Delta_{1,2} = 2|V_{12}| \quad (\text{A.12})$$

because the eigenvalues E for the perturbation equation $(\mathcal{H}_0 + V)\psi = E\psi$ is given as

$$E = \frac{1}{2}(U_1 + U_2 + U_{11} + U_{22}) \pm \sqrt{\frac{1}{4}(U_1 - U_2 + U_{11} - U_{22})^2 + |V_{12}|^2} \quad (\text{A.13})$$

Summarizing eqs. (A.8), (A.11) and (A.12), we get a probability of a state which is initially in the state ψ_1 remains in ψ_1 through the QTM with the sweeping rate $c = dH/dt$ as

$$|a_1(-\infty)|^2 = \exp\left(-\frac{\pi\Delta_{1,2}^2}{2\hbar c g\mu_B |m_1 - m_2|}\right) \quad (\text{A.14})$$

Then the probability of a state which is initially in the state ψ_1 changes to ψ_2 through the QTM is expressed as

$$1 - |a_1(-\infty)|^2 = 1 - \exp\left(-\frac{\pi\Delta_{1,2}^2}{2\hbar c g\mu_B |m_1 - m_2|}\right) \quad (\text{A.15})$$

Appendix B

Measurement of capacitance

B.1 Three terminal method

Most physical capacitors can be accurately represented by the three capacitances shown in Fig. B.1:

- The direct capacitance, C_{HL} , between the terminals H and L (capacitance between the plates of the capacitor),
- The two terminal capacitances, C_{HG} and C_{LG} , capacitances from the corresponding terminals and plates to the capacitor box, surrounding objects and to ground.

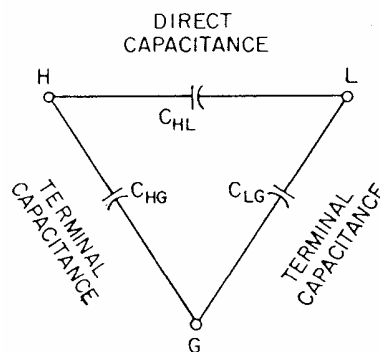


Figure B.1.1: Schematic diagram of a capacitor showing the direct capacitance and its associated terminal capacitances.

In the two terminal connections, the capacitor has the L and G terminals connected together, i.e., the L terminal is connected to the box. The terminal capacitance, C_{LG} , is thus shorted, and the total capacitance is the sum of C_{HL} and C_{HG} . Since one component of the terminal capacitance C_{HG} is the capacitance between the terminal and the surrounding objects, the total capacitance can be changed by changes in the environment of the capacitor and particularly by the wires connected to the capacitor. Therefore, for small capacitances or for higher accuracy the two terminal method is not practical.

A three terminal capacitor (Fig B.2) has connected to the G terminal a shield which completely surrounds the terminals, its connecting wires, and its plates except for the area

that produces the desired direct capacitance (terminal H and L). Changes in the environment and the connections can vary the terminal capacitances, C_{HG} and C_{LG} , but the direct capacitance C_{HL} – usually referred to simply as the capacitance of the three terminal capacitor – is determined only by the internal geometry.

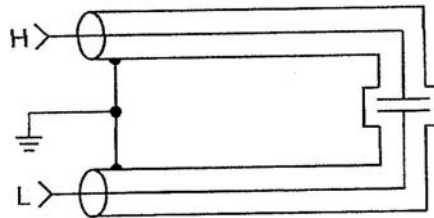


Figure B.1.2: Diagram of three terminal capacitor

The direct capacitance can be made as small as desired, since the shield between terminals can be complete except for a suitably small aperture. The losses in the direct capacitance can also be made very low because the dielectric losses in the insulating materials can be made a part of the terminal impedances.

B.2 Basic bridge circuits

Most of the measurements of capacitance are made by a null method which uses some form of the basic ratio bridge, shown in Fig. B.2.1. The capacitance of the unknown capacitor, C_X , is balanced by a calibrated, variable, standard capacitor, C_N , or by a fixed standard capacitor and a variable ratio arm, such as R_A . Such bridges with resistive ratio arms and with calibrated variable capacitors or resistors can be used over a wide range of both capacitance and frequency.

For higher accuracy (more than 0.1%), resolution and stability, a bridge with inductively coupled or transformer ratio arms has many advantages. A simple capacitance bridge like this is shown in Fig. B.2.2. On the toroidal core, a primary winding, connected to the generator, serves only to excite the core; the number of primary turns, N_p , determines the load on the generator but does not influence the bridge network.

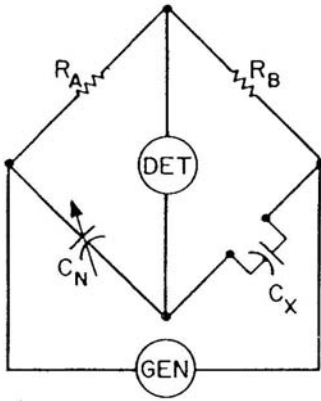


Figure B.2.1: Basic ratio bridge.

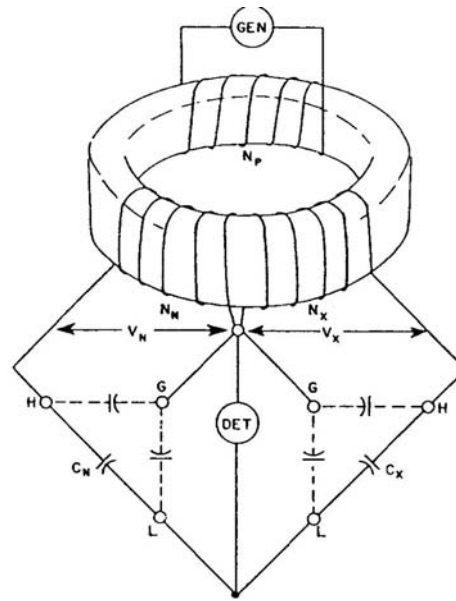


Figure B.2.2: A capacitance bridge with transformer ratio arms.

secondary windings (N_N , N_X) are used as the ratio arms of the capacitance bridge with the standard capacitor, C_N , and the unknown, C_X , as the other two arms in a conventional four arm bridge network. The condition for balance, or zero detector current, is shown to be

$$V_N C_N = V_X C_X \rightarrow \frac{C_X}{C_N} = \frac{V_N}{V_X} = \frac{N_N}{N_X}. \quad (\text{B.2.1})$$

There are some possible ways of balancing a simple transformer ratio capacitance bridge, like two equal ratio arms and C_N as a variable capacitor, or a fixed capacitor and one variable arm (changing N_N)

B.3 Basic bridge circuit of AH2550A Capacitance Bridge

The basic bridge circuit of AH2550A Capacitance Bridge is shown in Fig. B.3.1.

A 1 kHz sine wave generator excites the ratio transformer which forms legs 1 and 2 of the basic bridge. Both of these legs have many transformer taps to allow selection of precisely defined voltages to drive legs 3 and 4 of the bridge. Leg 3 consists of one of several fused-silica capacitors plus other circuitry that simulates a very stable resistor. Leg 4 contains the unknown impedance. The microprocessor in the AH2550A performs

the task of selecting (or balancing) Taps 1 and 2 of the transformer and of selecting C_0 and R_0 so that the voltage present at the detector is minimized. The detector is capable of detecting both in-phase and quadrature voltages with respect to the generator voltage. This allows both resistive and capacitive components of the unknown impedance to be independently balanced. If the microprocessor is able to obtain this null (minimum voltage) condition, the unknown capacitance can then be determined since the ratio of the unknown capacitance (C_X) to C_0 is equal to the ratio of the voltage on Tap 1 to the voltage on Tap 2 (see Eq. B.2.1 where $C_0 \equiv C_N$).

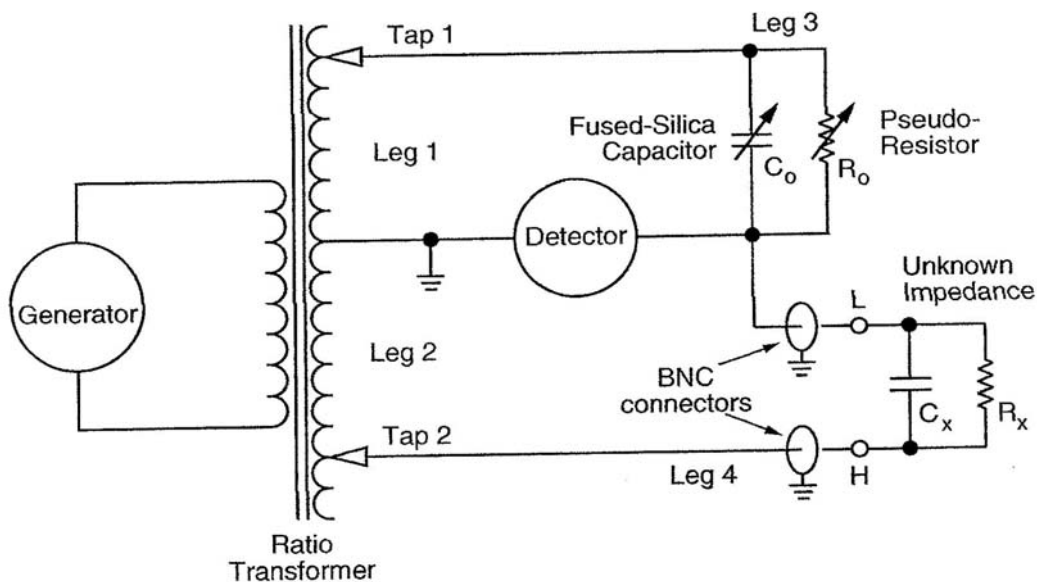


Figure B.3.1: Basic bridge circuit of AH2550A Capacitance Bridge.

Appendix C

The force that acts on the load cell

The leading term of the actual z component of the vertical field gradient is

$$\frac{\partial B}{\partial z} \equiv G_0. \quad (\text{C.1})$$

Although the fields produced by the magnet may be axially symmetric, the condition $\text{div } \mathbf{B} = 0$ leads to a radial component of the field of order:

$$B_r = -rG_0/2 \quad (\text{C.2})$$

In cases where the sample is anisotropic, \mathbf{M} is not always parallel to the field \mathbf{B} , and may have a small radial (perpendicular to \hat{z}) component M_r . I assume $M_r \ll M_z \approx |\mathbf{M}|$. Neglecting terms proportional to $\partial B_z / \partial r$, the force will then be

$$\begin{aligned} F_z &= M_z G_0 \\ F_r &= -M_r G_0 / 2 \end{aligned} \quad (\text{C.3})$$

for the axial and radial components, respectively. The component F_r is important for the lateral instability effect in the case of the faraday balance [37]. In addition to the force, the sample will experience a torque

$$\boldsymbol{\tau} = \mathbf{M} \times \mathbf{B} \quad (\text{C.4})$$

All these forces and torques contribute to the displacement of the capacitor plate, and the response δ can be written to a first approximation as

$$\delta = uF_z + vF_r + w|\boldsymbol{\tau}| \quad (\text{C.5})$$

where the coefficient u , v , and w depend on the particular design of the load cell. The devices used in previous experiments [11,38] were made of a simple cantilever or a diaphragm. These types of capacitors showed a rather strong response to the torque.

As a result, evaluation of \mathbf{M} became troublesome in the case of anisotropic materials, since N strongly depends on a minor misalignment of the sample and is therefore not reproducible.

The load cell in this experiment was designed by the load cell of Sakakibara et al [27]. Their movable plate was supported by two pairs of crossed wires of phosphor bronze, stung from the x- and y-directions with a small tension of $\sim 0.1\text{N}$, 3mm apart along the \hat{z} axis. This structure enabled the plate to move flexibly only along the z direction, keeping

its face parallel to the fixed plate. They have checked that in this design, the load cell is much less susceptible to the torque as well as to the radial force. In our design, the movable plate was attached to the wires (the casting of the stycast was formed on the wires) and by that we reached bigger stability.

If we summarize all this reasons:

- $M_r \ll M_z \approx |\mathbf{M}|$
- $B_r \ll B_z$
- The specific design of the cell cause to $v, w \sim 0$

We get that we can neglect the torque and the radial force:

$$\delta = v M_z \frac{\partial B_z}{\partial z} \quad (\text{C.6})$$

and if $\delta = \varepsilon_0 A (C_0^{-1} - C^{-1})$ were $C = C_0 + \Delta C$ so:

$$C_0^{-1} - C^{-1} = a \cdot M_z \frac{dB_z}{dz} \quad (\text{C.7})$$

were $a = v / \varepsilon_0 A$.

Appendix D

Decrease in asymmetry between the sample and holder measurements

In the MuSR measurements we noticed, by measuring samples of increasing size, that the amplitude of the muon rotation decreased. This led us to a speculation that muons that enter the sample relax immediately, and we are actually observing only the muon that missed the sample and landed in the sample holder. Since Fe8 is a ferromagnet, the field it creates outside the crystal depends on the average polarization of the molecules, and it is this average that we detect.

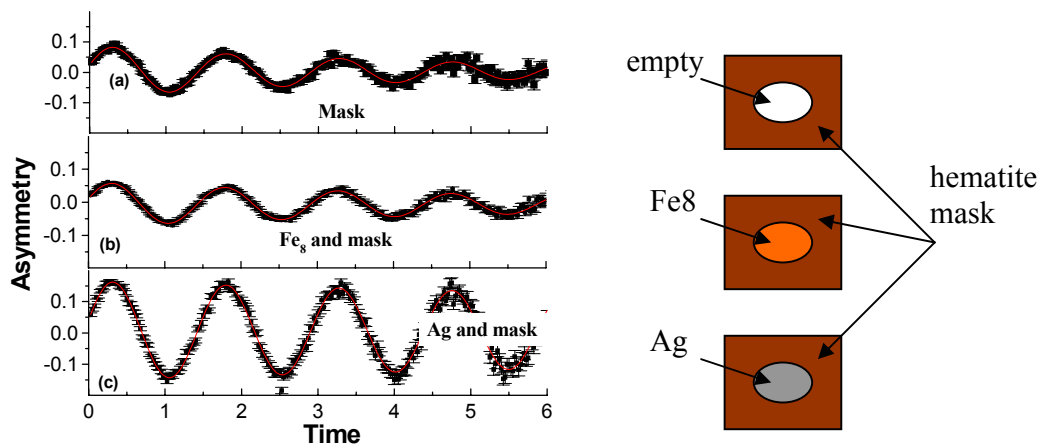


Fig. D.1: A demonstration that Fe8 depolarize muons immediately. The asymmetry of a hematite and glue mask (a) is very similar to mask and Fe8 (b), but different from mask and silver (c). Therefore, muons in Fe8 do not contribute asymmetry.

In order to check this hypothesis we performed three tests: (I) we measured (see Fig D.1a) the asymmetry $A_0=0.084$ of a mask, made of hematite (Fe_2O_3) and glue with a hole in its centre, using a Vito counter (muons that missed the mask do not contribute);

(II) when covering the hole with Fe8 we found (see Fig D.1b) $A_0=0.067$; and (III) replacing the Fe8 with silver gave (see Fig. D.1c) $A_0=0.157$. Muons that stop in silver do not relax and give $A_0=0.24$, while in hematite they relax immediately ($A_0=0$). Therefore, we can estimate the ratio of the muons that hit the mask (N_m) and silver (N_s) from

$$\frac{N_m}{N_m + N_s} \cdot 0.067 + \frac{N_s}{N_m + N_s} \cdot 0.24 = 0.157, \text{ to be } N_m / N_s = 1. \text{ Since we expect } N_{fe8} = N_s,$$

where N_{fe8} is the number of muons that hit Fe 8, we find from Fig. 5.1.1b that in Fe8 $A_0=0.02$. This is consistent with zero since there is some GE varnish on the Fe8. We therefore conclude that muons in Fe8 relax immediately as they do in hematite.

References

1. C. Sangregorio, T. Ohm, C. Paulsen, R. Sessoli, D. Gatteschi, *Phys. Rev. Lett.*, 78 (1997) 4645.
2. A. Barra, P. Debrunner, D. Gatteschi, Ch. E. Schulz and R. Sessoli, *Euro. Phys. Lett.* 35 (1996) 134.
3. J. G. E. Harris and D. D. Awschalom, *Physics World* 12 (1999), 19.
4. S.H. Kilcoyne, S.L. Lee, R. Cywinski, "Muon Science", SUSSP and Institute of Physics Publishing, Bristol, 1998.
5. A. Caneschi, D. Gatteschi, C. Sangregorio, R. Sessoli, L. Sorce, A. Cornia, M.A. Novak, C. Paulsen, W. Wernsdorfer, *JMMM*, 200 (1999) 182-201.
6. K. Wieghardt, K. Pohl, I. Jibril and G. Huttner, *Angew. Chem. Int. Ed. Engl.* 23 (1984), 77.
7. C. Delfs, D. Gatteschi, L. Pardi, R. Sessoli, K. Wieghardt and D. Hanke, *Inorg. Chem.* 32 (1993), 3099.
8. R. Caciuffo, G. Amoretti, A. Murani, R. Sessoli, A. Caneschi, D. Gatteschi, *Phys. Rev. Lett.*, 81(21) (1998), 4744-4747; Yves Pontillon, A. Caneschi, D. Gatteschi, R. Sessoli, E. Ressouche, J. Schweizer, E. Lelievre-Berna, *J. Am. Chem. Soc.* 121 (1999), 5342-5343
9. M. Ueda, S. Maegawa, H. Miyasaka & S. Kitagawa, *J. Phys. Soc. Jpn.* 70 (2001), 3084.
10. M. Ueda, PhD thesis, Kyoto University, 2001.
11. W. Wernsdorfer, R. Sessoli, A. Caneschi, D. Gatteschi, A. Cornia, D. Mailly, *J. Appl. Phys.* 87 (2000), 5481.
14. M. N. Leuenberger, D. Loss, *Nature*, 410 (2001), 789.
13. N. Prokofév and P. Stamp. *J. Low Temp. Phys.* 104 (1996), 143.
14. D. Gatteschi, R. Sessoli, *Angew. Chem. Int. Ed.* 42 (2003), 268.
15. J. Villain, A. Fort, *J. Euro. Phys. B.* 17 (2000), 69.

16. R. Caciuffo, G. Amoretti, A. Murani, R. Sessoli, A. Caneschi and D. Gatteschi, *Phys. Rev. Lett.* 81 (1998), 4744.
17. E.M. Chudnovsky, D.A. Garanin, *Phys. Rev. Lett.*, 87 (2001), 187203.
18. C. Zenner. *Proc. Roy. Soc. London A*, 137 (1932), 696.
19. L. Landau, *Phys. Z. Sowjetunion.* 2 (1932), 46.
20. E.C.G. Stückelberg, *Helv. Phys. Acta.* 5 (1932), 369.
21. W. Wernsdorfer, R. Sessoli, *Science* 1999, 284, 133.
22. W. Wernsdorfer, *cond-mat/0101104* (2001).
23. E. Rastelli, A. Tassi, *Physical Review B*, 64 (2001), 064410.
24. K. Wieghardt, K. Pohl and W. Gebert, *Angew. Chem. Int. Ed. Engl.* 22 (1983), 722.
25. H. London, G.R. Clarke, E. Mendoza, *Phys. Rev.* 128 (1962), 1992.
26. "Partical Cryogenics – An introduction to laboratory cryogenics", Oxford Instruments, (1996).
27. T. Sakakibara, H. Mitamura, T. Tayama and H. Amitsuka, *Jpn. J. Appl. Phys.* 37 (1994) 5067.
28. H. Zijlstra, "Experimental methods in magnetism", North Holland Publishing Company, Amsterdam, 1967, Vol. 2, Chap. 3.
29. A. G. Swanson, Y. P. Ma, J. S. Brooks, R. M. Markiewicz, N. Miura, *Rev. Sci. Instrum.*, 61 (2) (1990), 848.
30. C.D. Anderson, S.H. Neddermeyer, *Phys. Rev.* 50 (1936), 263.
31. A. Keren. PhD thesis, Colombia University, 1994.
32. J. H. Brewer, R. Cywinski, "Muon Science – Muons in Physics, Chemistry and Materials" edited by S. L. Lee, S. H. Kilcoyne and R. Cywinski, page 1 (1998).
33. S. J. Blundell, *Contemporary Physics*, 40 (1999), 175.
34. T. Ohm, C. Sangregorio, C. Paulsen, *J. Low Temp. Phys.* 113 (1998), 1141; T. Ohm, C. Sangregorio, C. Paulsen, *Eur. Phys. J. B* 6 (1998), 195
35. Z. Salman. PhD thesis, Technion, 2002.
36. Z. Salman, A. Keren, S. Megeawa, M. Ueda, O. Shafir, B. Barbara, C. Baines, *Physica-B*, 326 (2003), 480.
37. A. M. Stewart, *J. Physics E*, 8 (1975), 55.

38. J.S. Brooks, M.J. Naughton, Y.P. Ma, P.M. Chaikin, R.V. Chamberlin, *Rev. Sci. Instrum.* 58 (1) (1987), 117.

**חקירת האופי הקוונטי של
המולקולות בעלות הספין
הגבוה Fe8 בעזרת μ SR**

אורן שפיר

חקירת האופי הקוונטי של המולקולות בעלות הספין

הגבוה Fe8 בעזרת μ SR

חיבור על מחקר

לשם מילוי חלקי של הדרישות לקבלת התואר מגיסטר למדעים

בפיסיקה

אורן שפיר

הוגש לסנט הטכניון – מכון טכנולוגי לישראל

שבט תשס"ד חיפה פברואר 2004

המחקר נעשה בהנחיית פרופ' עמית קרן בפקולטה לפיסיקה בטכניון.

אני מודה מקרב לב לפרופ. עמית קרן על הדרכתו המעולה, תמיכתו ועידודו לאורך כל התקופה.

אני מודה לפרופ. פולטורק ולפרופ. רזניקוב על עזרתם עם ה-DR. אני מעריך מאוד את עזרתם של דר. שינין, דר. קפון ופרופ. כפתורי בהכנת הדגמים ואפיונם. תודה גדולה לפרופ. מיאגאווה ודר. יואדה עבור הדגמים הראשונים ולדר. יואדה עבור עזרתה בכתיבת התיזה. עבור עזרה במתקני ה- μ SR תודתי נתונה לדר. אמאטו ולמר ביינס.

הוקרה מיוחדת על עזרתם הגדולה של הטכנאים – גלינה, שמואל, מרדכי ודר. לאוניד אומין. כמו כן תודה לדר. סלמאן על עזרתו בשלבים הראשונים.

תודה לכל חברי בקבוצות המחקר מגנטיות וטמפרטורות נמוכות – דר. עמית קניגל, אווה, רינת, שחר, אריאל, אושרי, מני וליאור על עזרתם ועל יצירת סביבת עבודה נפלאה.

תודה מיוחדת לבלהה, זאת שעמדה לצידי ובזכותה התקופה הזו היתה יותר מסתם תקופת לימודים בעבורי.

אני מודה לטכניון על התמיכה הכספית בהשתלמותי.

להורי, ניסים ותמי, על אהבתם ותמיכתם ללא סייג

תוכן עיניינים

-1-	תקציר
-3-	רשימת קיצורים וראשי תיבות
-5-	1. מבוא
-5-	1.1 הקדמה – מולקולות העלות ספין גבוה
-5-	1.2 מנהור קוונטי של המגנטיזציה (מק"מ) ב- Fe8
-8-	1.3 מוטיבציה לעבודת המחקר
-10-	2. מנהור קוונטי במולקולות בעלות ספין גבוה
-10-	1.1 מנהור בין מצבים מנוונים
-11-	1.3 H_0 ורלקסציה מגנטית
-12-	1.4 תהליך המנהור
-14-	1.5 מנהור בשדות מגנטיים חיצוניים
-15-	1.6 השיטה של לנדאו וזנר
-17-	3. שיטות ניסיוניות
-17-	3.1 הכנת הדגם
-18-	3.1.1 אנליזה כימית
-18-	3.1.2 אנליזה גבישית באמצעות קרינת X
-19-	3.2 מקרר דילול
-22-	3.3 מגנטומטר כוח פארדי
-22-	3.3.1 שיטת המדידה
-23-	3.3.2 עיצוב וביצועים של תא המטען
-26-	3.4 טכניקת רוטצית ספין מיואון (μ SR)
-26-	3.4.1 מבנה הניסוי

-28-	תצורת השדה הרוחבי	3.4.2
-28-	ניתוח הנתונים	3.4.3
-31-	רוטציה של ספין מיואון	3.4.4
-32-	4. תוצאות ניסיוניות	
-32-	4.1 ניסוי במגנטומטר כוח פארדי	
-32-	4.1.1 גביש יחד של Fe8	
-34-	4.1.2 קובץ גבישים של Fe8	
-35-	4.1.3 ניתוח תוצאות הניסוי במגנטומטר כוח פארדי	
-37-	4.2 ניסוי μ SR	
-37-	4.2.1 מבנה הניסוי	
-39-	4.2.2 מיואונים פוגעים בפלטת הכסף - תוצאות	
-41-	4.2.3 מיואונים פוגעים בפלטת הכסף - ניתוח תוצאות	
-42-	4.2.4 מיואונים פוגעים ב-Fe8 - תוצאות	
-43-	4.2.5 מיואונים פוגעים ב-Fe8 - ניתוח תוצאות	
-45-	5. דיון וסיכום	
-45-	5.1 השוואה למודל לנדאו זנר ולניסויים אחרים	
-49-	5.2 ההבדל בין Fe8 לבין מגנט רגיל	
-50-	5.3 סיכום	
	נספחים	
-52-	A – מעברים לא אדיאבטיים המוסברים בעזרת לנדאו וזנר	
-55-	B – מדידת קיבול	
-59-	C – הכוח הפועל על תא המטען	
-61-	D – הירידה באסימטריה בין המדידות של הדגם ומחזיק הדגם	
-63-	רשימת מקורות	
- י -	תקציר בעברית	

רשימת איורים

- 1.2.1** המבנה של הנו-מגנט המולקולה Fe8: (a) מבט מולקולרי – סכימת חיצים של מבנה הספינים [5]; (b) צורת הגביש – מבט סכימטי של גביש Fe8 והצירים המרכיבים את תא היחידה.
- 1.2.2** התלות בסחיפה של טמפרטורה (a) ושדה מגנטי (b) של לולאות היסטריזיס של צברים מולקולריים של Fe8. מנהור תהודתי נצפה באמצעות מדרגות המרוחקות זו מזו בצורה שווה של $\Delta H_z = 0.22$ T, כאשר, ב- $T = 360$ mK, מתאימות למעברי מנהור מהמצב $M = -10$ למצבים $M = 10 - n$ כאשר $n = 0, 1, 2, \dots$. רוחב הרזוננס של כ- 0.05 T נובע בעיקר משדות דיפולריים של הצברים המולקולריים (מתוך [11]).
- 1.2.3** מצבי ספין במולקולת Fe8 ב- $H = 2D/g\mu_B$ (הקו שלם) ובשדה אפס (קו מקווקו).
- 1.3.1** המשקל האטומי של אלמנט זיכרון טיפוסי כפונקציה של הזמן (שנים) [29,31].
- 2.2.1** רמות אנרגיה עבור מצבי ספין S אנאיזוטרופיה מגנטית בציר הקל. רמות ה- M ממוקמות בצד השמאלי ורמות ה- $-M$ בצד הימני. (a) בשדה אפס שני הבורות מאוכלסים באופן שווה. (b) שדה מגנטי סלקטיבי מאכלס את הבור הימני. (c) אחרי הסרת השדה החזרה לשיווי משקל מתרחשת דרך סדרת שלבים [14].
- 2.3.1** "קיצור" אפשרי לרלקסציה המגנטית דרך מנהור בין מצבים מעוררים תרמית.
- 2.4.1** דיאגראמת זימן של 21 המצבים של Fe8 עם $S = 10$ כפונקציה של השדה המגנטי שהושם במקביל לציר הקל. מהתחתית ללמעלה, הרמות מסומנות במספרים הקוונטיים $M = \pm 10, \pm 9, \dots, 0$. הצטלבות בין הרמות מתקבלת בשדות המקיימים $\mu_0 H_z = n \cdot 0.22$ T עם $n = 1, 2, 3, \dots$. בגרף הקטן ניתן לראות הגדלה של ההצטלבות כאשר הרכיבים הרוחביים (שמכילים את אופרטורי הספין S_x או S_y) הופכים את ההצטלבות ל"????". ככל שהפער $\Delta_{m,m'}$ גדול יותר, קצב המנהור מתגבר. [11]
- 3.1.1** תמונה של גבישי Fe8.
- 3.1.2** מבט סכמטי של גביש יחיד של Fe8 והצירים הקריסטלוגרפיים –
 $\alpha = 89.64^\circ$ $\beta = 109.99^\circ$ $\gamma = 109.20^\circ$ - $a = 10.64 \text{ \AA}$, $b = 14.12 \text{ \AA}$, $c = 15.09 \text{ \AA}$
- 3.2.1** דיאגראמת פאזות של ${}^3\text{He}/{}^4\text{He}$.
- 3.2.2** דיאגראמה סכמטית של מקרר דילול.
- 3.3.1** עיקרון המדידה. הכוח המגנטי F פועל על דגם המוצב בשדה משתנה מרחבית נמדד באמצעות השינוי בקיבול של קבל לוחות משתנה, כאשר הפלטה הנעה שלו מוצבת על קפיצים אלסטיים S.

- 3.3.2** מבט בחתך צד על תא המטען. הפלטה הנעה מוחזקת האמצעות 4 חוטים העשויים מתרכובת של ברונזה וזרחן. הקוטר של הלוחות הוא 16 מ"מ.
- 3.3.3** התגובה של תא המטען למשקל בטמפרטורת החדר.
- 3.3.4** מבט סכמטי על התקן תא המטען, המותקן שלא במרכז הסליל היוצר את השדה המגנטי, בתוך מקרר הדילול.
- 3.4.1** (a) איור סכמטי של דעיכת פיון חיובי למיזאון וניוטרינו. [31] (b) תמונת מראה של דעיכת מיזאון. הכיוון של ספין המיזאון הוא הפוך בתמונת המראה כך שהפוזיטרונים נפלטים בכיוון מועדף המנוגד לספין המיזאון. בגלל עיקרון שמירת הזוגיות, בעולמנו מתרחש רק התהליך שבצד שמאל בדיאגרמה.
- 3.4.2** התפלגות זוויתית של הפוזיטרונים הנפלטים עקב דעיכת מיזאון עבור אנרגיות שונות של הפוזיטרון.
- 3.4.3** מבנה המערכת בשדה רוחבי.
- 3.4.4** סימולציה של ספקטרום גולמי של פוזיטרונים בגלאים הקדמי והאחורי (a) עבור גאומטריה של שדה רוחבי (TF) ושדה אורכי (LF) ביחד עם ספקטרום האסימטריה המתוקנת (b). [32]
- 3.4.5** הקיטוב של המיזאון $P(t)$ בנוכחות שדה מגנטי קבוע B .
- 4.1.1** הקיבול (ביחידות אקראיות) כנגד השדה המגנטי בשמונה קצבי סחיפה שונים (ב- 40 mK).
הקווים המקווקווים האנכיים מסמנים בקירוב את השדות המתאימים $H_m \approx n \times 2.2T$.
- 4.1.2** הקיבול כנגד השדה המגנטי ($dH/dt=0.15T/min$, Temp=40mK). ניתן לראות שהמרחק בין מדרגות הוא כמעט קבוע (כל החיצים באורך אחיד).
- 4.1.3** הקיבול (ביחידות אקראיות) כנגד השדה המגנטי בארבע טמפרטורות שונות (קצב סחיפה קבוע של $0.15T/min$). הקווים המקווקווים האנכיים מסמנים בקירוב את השדות המתאימים $H_m \approx n \times 2.2T$.
- 4.1.4** הקיבול כנגד השדה המגנטי בחמישה קצבי סחיפה שונים (ב- 40 mK). ניתן להבחין שככל שקצב המנהור מהיר יותר, הקפיצה מופיעה בשדה נמוך יותר.
- 4.1.5** גובה הקפיצה (ב- 0.17T) כפונקציה של קצב הסחיפה. הקו הרציף כמנחה לצופה.
- 4.2.1** הסידור של גבישי ה-Fe8 במערכת הניסויית [21].
- 4.2.2** (a) בניסוי הראשון המיזאונים פוגעים בפלטת הכסף, בעוד שבניסוי השני (b) חלק מהם עוצרים בדגם או בדבק (G-varnish) שבין הגבישים.
- 4.2.3** מדידות μSR בגבישי Fe8 (מיזאונים פוגעים בכסף). שדות אמצעיים שונים מובילים לתדירויות שונות של רוטציה המיזאון, במיוחד בין $H_i=0.2T$ (-0.2T) ל- $H_i=0.3T$ (-0.3T).
- 4.2.4** מדידות μSR בדגם ריק (מיזאונים פוגעים בפלטת הכסף). שדות אמצעיים שונים מובילים לתדירויות שונות של רוטציה המיזאון בשדות נמוכים ולדומות בשדות גבוהים.
- 4.2.5** ההסטה בתדירות רוטציה המיזאון כפונקציה של השדות האמצעיים H_i , בין מחזיק דגם ריק ו- Fe8. נתונים גולמיים של ω כנגד H_i מוצגים בגרף הקטן. הקו המלא משמש כמנחה לצופה.

- 4.2.6** מדידות μSR בגבישי Fe8 (מיואונים פוגעים בדגם). שדות אמצעיים שונים מובילים לתדירויות שונות של רוטציית המיואון ב-Fe8 (a, b & c) אך לתדירויות דומות במחזיק הריק (d, e & f).
- 4.2.7** ההסטה בתדירות רוטציית המיואון (ומכאן השדה המגנטי שהוא חש) כפונקציה של השדות האמצעיים H_i , בין מחזיק דגם ריק ו-Fe8. נתונים גולמיים של ω כנגד H_i מוצגים בגרף הקטן. הקו המלא משמש כמנחה לצופה.
- 5.1.1** התלות בקצב סחיפת השדה של הפיצול המינהורי הנמדד על שיטת לנדאו-זנר (a). ההסתברות למינהור המדודה P מצויינת במספר קצבי סחיפה. ב- (b) מוצג הפיצול המינהורי כפונקציה של השדה הרוחבי עבור $\varphi=0^\circ$ (במקביל לציר הקשה), ולמעברי קוונטיים בין $M = -10$ ו- $(S - n)$. [21, 11]
- 5.1.2** דיאגרמה סכמטית של הסיכוי למנהור מ- $m=-10$ ל- $m=10,9$, במהלך הניסוי במחזור משולש של שדות, עם $0.2T < H_i < 0.4T$. ההסתברות לאי-מינהור ניתן ע"י $(1-P_{-10,10}) \times (1-P_{-10,9})^2$.
- 5.1.3** תוצאות ניסוי ה- μSR ב-Fe8 $(\Delta\omega_\infty - \Delta\omega_0) / (2\Delta\omega(H_i) - \Delta\omega_0 - \Delta\omega_\infty)$ כאשר הקו המנוקד הוא כמדריך לצופה, ותחזית תיאורטית (קו מלא כחול) על פי מודל לנדאו וזנר, $P_{up}(H_i) - P_{down}(H_i)$. המדרגות מופיעות במיקום הנכון אך בגובה שונה.
- 5.1.4** לולאות היסטוריס שנמדדו ע"י וורנסדורפר בנוכחות שדה רוחבי קבוע ב- $0.04K$. נלקח ממקור [11].
- 5.2.1** אותו הניסוי ($1.5T \leftarrow H_i \leftarrow 0.005T$) נעשתה ב- SmCo (a), מגנט קבוע רגיל בעל שדה רוויה דומה. ניתן לראות מישור יחיד בניגוד ל-Fe8 שבו רואים בין שניים לשלושה אזורים יציבות (b).
- A.1** הצטלבות של רמות אנרגיה.
- B.1.1** דיאגרמה סכמטית של קבל המראה את הקיבול הישיר ואת קיבולי המסופים המקושרים.
- B.1.2** דיאגרמה של קבל בעל שלושה מסופים.
- B.2.1** גשר יחס בסיסי.
- B.2.2** גשר קיבול עם זרועות יחסיות בשנאי.
- B.3.1** גשר קיבול בסיסי של גשר הקיבול AH2550A.
- D.1** הדגמה המראה כי Fe8 מבטל את קיטוב המיואונים באופן מידי. האסימטריה של תחמוצת ברזל ומסיכת דבק (a) דומה מאוד למסכה עם Fe8 (b), אך שונה ממסכה וכסף. מכאן, ש-Fe8, בדומה לתחמוצת ברזל, לא תורם לאסימטריה.

רשימת טבלאות

- 3.1.1 תוצאות המיקרו-אנליזה הכימית של Fe8.
- 3.1.2 תוצאות האנליזה הקריסטלוגרפית של קרינת X.

תקציר

צברים של מולקולות המכילות יוני מתכת פאראמגנטיים, נמצאים במחקר נרחב כמודל למגנטיות בסקלה הנומטרית, במיוחד בגלל האפקטים הקוונטים כמו המנהור של המומנט המגנטי. המולקולה המגנטית $[(C_6H_{15}N_3)_6Fe_8O_2(OH)_{12}]Br_7(H_2O)Br \cdot 8H_2O$, או בקיצור Fe_8 , היא תרכובת מייצגת שבה התגלה מנהור קוונטי של המגנטיזציה (QTM), ועבודת מחקר זו מתרכזת בה.

שדה מחקר זה הפך למעניין יותר בגלל היישומים העתידיים של מולקולות אלו. הטכנולוגיה היום הגיעה לנקודה שבה ניתן להשפיע על אטום בודד או מולקולה בודדת, ובכך מאפשרת הקטנת יחידת הזיכרון המגנטי מהגודל הנוכחי של 10^8 אטומים לביט (יחידת זיכרון) [3], למולקולה בודדת. הקושי הוא ביציבות של המידע המאוכסן – הקיטוב של הספין (כלומר הזיכרון המאוכסן במולקולה בודדת) יכול ללכת לאיבוד בגלל מינהור קוונטי. כתוצאה מכך, ישנו מאמץ נרחב להבין את המכניזם של המנהור הקוונטי המגנטי בתקווה למנוע אותו ביום מן הימים. בנוסף לכך ישנו מאמץ מתמשך לייצר שכבות דקות של Fe_8 . ברגע שמטרה זו תושג, יהיה צורך לאשר שהמולקולות בשכבות הדקות מתנהגות בדומה למולקולות בגבישים גדולים. זוהי לא משימה פשוטה כיוון שמדידות שנעשו עד היום כמו מדידות סוספטביליות, תהודה מגנטית גרעינית (NMR), קיבול חום וכולי, דורשות דגם בנפח גדול ואינן יכולות להיות מיושמות על שכבות דקות.

המולקולה Fe_8 שייכת לקבוצה של מולקולות בעלות ספין גבוה. מולקולות אלה מסתדרות על שריג כאשר המרחק בין מולקולות שכנות גדול כך שבטמפרטורות הנמוכות מגודל האינטראקציה בין היונים (J), המולקולות מתנהגות כמו ספינים גדולים בלי אינטראקציה ביניהן. כל מולקולה של Fe_8 מכילה 8 יוני ברזל Fe^{+3} (בעלי ספין של 5/2), שהאינטראקציה ביניהם אנטיפרומגנטית. התכונות המגנטיות של המולקולה הוסברו ע"י מודל פשוט עם ספין כולל $S=10$ הבנוי משישה ספינים מקבילים אחד לשני והשניים הנותרים בכיוון אנטי-מקביל לשאר (מודל זה אומת במדידות של פיזור נויטרונים [8]). התוצאות הניסיוניות של מדידות מגנטיות בטמפרטורות נמוכות מראות אנאיזוטרופיה התלויה בכיוון השדה המגנטי ביחס לצירי הגביש.

כאשר למולקולה יש אנאיזוטרופיה מגנטית לאורך ציר z ניתן לרשום את המילטוניאן הספין של מולקולה בודדת בשדה מגנטי H_z בצורה:

$$\mathcal{H} = DS_z^2 + g\mu_B H_z S_z$$

כאשר D הוא הגודל המתאר את גודל האנאיזוטרופיה, S_z הוא רכיב הספין של המולקולה בכיוון z, $g = 2$, μ_B הוא קבוע המגנטון של בוהר, ו- $g\mu_B H_z S_z$ הוא איבר זימן. לכן ללא שדה מגנטי מצבי האנרגיה של ספין מעלה (בכיוון +z) וספין מטה (בכיוון -z) תהיה שווה. בטמפרטורות גבוהות (מעל לגודל האנאיזוטרופיה של המולקולה) הספין של המולקולה יכול להתהפך ממצב מעלה למצב מטה ולהיפך ע"י מעבר

תרמי מעל למחסום האנאיזוטרופיה, אבל כאשר הטמפרטורה נמוכה בהרבה ממחסום זה, הערוץ היחיד האפשרי למעבר בין מצבי הספין הוא ע"י מנהור קוונטי. המינהור בין מצבי ספין שונים אפשרי כאשר בהמילטוניאן של הספין מופיע ביטוי נוסף שאינו מתחלף עם רכיב הספין S_z , במקרה שלנו $E \cdot (S_x^2 - S_y^2)$. התנהגות זו מעניינת כי היא מאפשרת לנו "לראות" תופעות קוונטיות ע"י מדידות מקרוסקופיות. זוהי התופעה הנקראת "מינהור קוונטי של המגנטיזציה".

המודל הפשוט ביותר מדבר על בור פוטנציאל כפול. אם פונקציות הגל של המצבים בבור חופפות, כלומר יש אינטראקציה בינהן, נוצר פיצול בין רמות האנרגיה המנוונות הנקרא "פיצול המינהור", ומסומן Δ_T . הסיכוי למנהור תלוי ביחס בין האנרגיה של פיצול המנהור לאנרגית המחסום בין הבורות. רמות האנרגיה המתאימות להמילטוניאן ניתנות לחישוב ע"י ליכסון המטריצה של $2S+1$ המצבים האפשריים. התוצאות מראות שרמות האנרגיה בנוכחות שדה מגנטי בכיוון הציר הקל (למיגנוט) נחצות בשדות מגנטיים מתאימים הניתנים לחישוב בסדר ראשון ע"י

$$H_m(n) = \frac{nD}{g\mu_B}$$

המעבר בין שני המצבים נדון בתחילה ע"י לנדאו וזנר, ויושם במנהור מצבי הספין ב-Fe8. הסתברות המנהור P כאשר סוחפים את השדה האורכי H_z בקצב קבוע באזור בו שתי רמות מצטלבות ניתן ע"י:

$$P = 1 - \exp\left[-\frac{\pi\Delta_{m,m'}^2}{4\hbar g\mu_B |m-m'| SdH/dt}\right]$$

כאשר m ו- m' הם המספרים הקוונטיים של הרמות, dH_z/dt הוא קצב סחיפת השדה ו- \hbar הוא קבוע פלנק. את התופעה של המינהור הקוונטי ניתן לראות במדידות מקרוסקופיות של המגנטיזציה כפונקציה של השדה. כאשר המערכת נמצאת בשדה מגנטי מתאים H_m (הצטלבות של רמות אנרגיה) יש מעבר של מצבי הספין במינהור וניצן לראות זאת ע"י שינוי חד במגנטיזציה. כאשר הרמות אינן מצטלבות, אין מצבי הספין נשארים קבועים וכן גם המגנטיזציה. הדבר מתבטא לבסוף בלולאת היסטריזיס מדורגת, כאשר ב-Fe8 גילו כי מתחת לטמפרטורה של 400mK הלולאה לא תלויה בטמפרטורה, כלומר מתרחש מנהור "טהור".

בעבודה זו מוצגות מדידות בשתי שיטות. בכל אחת מהן קורר הדגם עד ל-40mK באמצעות מקרר דילול העובד על עיקרון של שאיבת ^3He מתערובת של $^3\text{He}/^4\text{He}$. הדגם הוצב כך שהציר הקל שלו יהיה תמיד מקביל לשדה המגנטי שהופעל בניסוי. שיטה אחת היא מגנטומטר כוח (בעיקרון פארדי) המודד מגנטיזציה על פי העיקרון שבו הדגם מפעיל כוח, השווה למכפלת המגנטיזציה בגרדיאנט השדה המגנטי, על קבל. מדידת הקיבול וידיעת הגרדיאנט נותנים את הערך של המגנטיזציה. בשיטה השנייה השתמשנו ברוטציית (סיבוב) ספין של מיואון – משתילים מיואונים חיוביים מקוטבים בתוך הדגם ומודדים את הקיטוב שלהם כפונקציה של הזמן. מכך ניתן להסיק מסקנות על המגנטיזציה של הדגם.

המדידות שבוצעו בשיטת מגנטומטר פארדי, הראו את האופי הקוונטי של המולקולה כפי שהיה ידוע מניסויים קודמים. מדידות המגנטיזציה בגביש יחיד הראו קפיצות בשדות המתאימים שהשתנו כפונקציה של קצב סחיפת השדה וכפונקציה של הטמפרטורה. המדידות בוצעו גם בקובץ של גבישים, על מנת להשוות מדידות אלו למדידות הרוטציה של ספין המיואון (שבוצעו גם על קובץ של גבישים). במדידות אלו ראינו קפיצה בודדת במגנטיזציה, המעידה על כך שלא כל הגבישים היו מכוונים כך שהציר המקביל שלהם יהיה מקביל לשדה המגנטי.

עיקר המחקר המוצג מתרכז במדידות שבוצעו על Fe8 בעזרת רוטציה של ספין מיואון. המולקולות קוטבו בשדה מגנטי חזק שלילי (1.5- טסלה), ולאחר מכן סחפנו את השדה לשדה אמצעי חיובי כלשהו (0.1-0.8 טסלה). לבסוף סחפנו את השדה לערך של 0.005 טסלה (ולא לאפס בדיוק כיוון שזה אחד מהשדות המתאימים בהם מתרחש מנהור קוונטי). כל המדידות התבצעו בשדה זה, וההבדל בין המדידות נבע מהשדה האמצעי, "ההיסטוריה" של הדגם. בעזרת המיואונים מדדנו את השדה המקומי שהם מרגישים כתוצאה מהספינים של מולקולות Fe8 בסביבתם, תוצאות המעידות בבירור על קיום תופעת המינהור הקוונטי של המגנטיזציה במולקולות אלה. ניתן לראות כי המיואון מבדיל בין ההיסטוריה השונה של כל דגם, כלומר השדה האמצעי שבו הדגם היה לפני המדידה, וזאת בניגוד למגנטים רגילים כגון SmCo. בשיטה זו ניתן "לרשום" ולאחר מכן "לקרוא" לפחות 4 מצבים יציבים במולקולה Fe8 לעומת שני מצבים בלבד במגנט רגיל. כאשר השונו את התוצאות הניסוי זה לניסויים קודמים ולמודל לנדאו-זנר, התגלתה אי התאמה בין גובה קפיצות בערך המגנטיזציה בניסוי לגודל הצפוי. על פי ניסויים קודמים, הקפיצה בשדה המתאים השלישי ($\sim 0.44T$) היתה צריכה להיות גבוהה יותר מזו שבשדה המתאים השני ($\sim 0.22T$). כיוון שתופעה זו נצפתה גם בניסוי המיואונים וגם בניסוי המגנטומטר כוח פארדי, אנו מסיקים כי הדגם ולא צורת המדידה הם הגורם לכך. אנו מעריכים כי ההסבר לכך הוא שחלק מהגבישים בצבר הנמדד לא היו מכוונים כך שהציר הקל שלהם יקביל לכיוון השדה המגנטי, מה שגרם לשדה בציר הקשה של הגביש והשפיע על התהליך כולו.

לסיכום, הראנו שמדידות ספין המיואון, שיכולות להיות מיושמות גם בשכבות דקות [4], רגישות לאופי הקוונטי של מולקולות Fe8. המדידות הראו ש-Fe8 יכול "לזכור" באיזה שדה אמצעי ביקרנו, וזיכרון זה נשמר לפחות בזמן המדידה שהיא כחצי שעה. למעשה, יש לנו תוצאות מהעבר שמראות שזיכרון זה נמשך לפחות מספר שעות. היכולת של ה-Fe8 "לזכור" את השדה האמצעי עורבת לכך שמולקולות אלה הן מועמדות ראויות לשמש כזיכרון מגנטי שיש בו יותר משני מצבים (לעומת זיכרון רגיל שהוא בינארי). אפשרות זו הוצעה בעבר ע"י Caneschi ושותפיו, אך על פי הידוע לנו לא הוצגה באופן ניסויני עד כה.